Accepted Manuscript

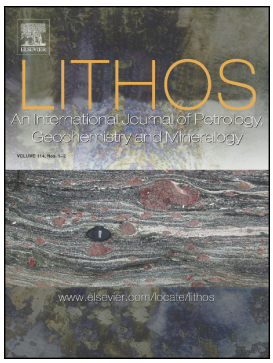

Neoarchean magmatic arc in the Western Liaoning Province, northern North China Craton: Geochemical and isotopic constraints from sanukitoids and associated granitoids

Jinghao Fu, Shuwen Liu, Peter A. Cawood, Maojiang Wang, Fangyang Hu, Guozheng Sun, Lei Gao, Yalu Hu

PII: S0024-4937(18)30389-X
DOI: doi:10.1016/j.lithos.2018.10.024
Reference: LITHOS 4840

To appear in: *LITHOS*

Received date: 21 May 2018
Accepted date: 22 October 2018

Please cite this article as: Jinghao Fu, Shuwen Liu, Peter A. Cawood, Maojiang Wang, Fangyang Hu, Guozheng Sun, Lei Gao, Yalu Hu , Neoarchean magmatic arc in the Western Liaoning Province, northern North China Craton: Geochemical and isotopic constraints from sanukitoids and associated granitoids. Lithos (2018), doi:10.1016/j.lithos.2018.10.024

Neoarchean magmatic arc in the Western Liaoning Province, northern North China Craton: Geochemical and isotopic constraints from sanukitoids and associated granitoids

Jinghao Fu[a], Shuwen Liu[a,*], Peter A. Cawood[b, c], Maojiang Wang[a], Fangyang Hu[a], Guozheng Sun[a], Lei Gao[a], Yalu Hu[a]

[a] *The Key Laboratory of Orogenic Belts and Crustal Evolution, Ministry of Education, School of Earth and Space Sciences, Peking University, Beijing 100871, PR China*

[b] *School of Earth, Atmosphere and Environment, Monash University, Melbourne, Victoria 3800, Australia*

[c] *Department of Earth and Environmental Sciences, University of St Andrews, St Andrews KY16 9AL, UK*

Corresponding author:

Shuwen Liu

School of Earth and Space Sciences, Peking University, Beijing 100871, China

Tel: 86-10-62754163

Fax: 86-10-62754163

Email: swliu@pku.edu.cn

Abstract

The Neoarchean Western Liaoning basement terranes in the northern part of North China Craton chiefly consist of tholeiitic basalts in the north, TTG gneisses and metavolcanic rocks in the northwest, and K-rich granitoids in the southeast. In the southeastern zone, porphyritic monzodioritic-quartz monzodioritic-granodioritic-monzogranitic (MQGM) gneisses are the major lithological assemblage, and locally contain minor xenoliths of TTG gneisses. Based on the major mafic mineral phases, the porphyritic MQGM gneisses can be divided into amphibole-dominated and biotite-dominated groups. Zircon U-Pb isotopic dating indicates that the amphibole-dominated MQGM gneisses, biotite-dominated MQGM gneisses, and tonalitic gneiss xenolith were emplaced during 2546-2529 Ma, 2546-2531 Ma, and at 2563 Ma, respectively. The 2563 Ma tonalitic gneiss xenolith displays geochemical affinities to high-SiO_2 adakites, and may be formed by the partial melting of descending oceanic slabs, with the melt contaminated by mantle peridotite. The amphibole-dominated MQGM gneisses are geochemically analogous to sanukitoids, and their magmatic precursors were formed by partial melting of lithospheric mantle, which was metasomatized by dehydration fluids and melts derived from subducted oceanic sediments and slabs. The magmatic precursors of the biotite-dominated MQGM gneisses were generated by the partial melting of medium-K to high-K mafic rocks at medium pressures. Integrated with previous studies on supracrustal sequences and granitoids in Western Liaoning Province, the Neoarchean lithological assemblages in the southeastern zone were most likely formed in an active continental margin setting.

Keywords: Sanukitoids and potassic granites; Petrogenesis; Neoarchean active continental margin; Western Liaoning Province; Northern North China Craton

1. Introduction

Granitoids are the dominant constituents of cratons, constituting more than 70% of the residual Archean crust (Moyen, 2011), thus providing an important probe into crustal formation and evolution. Archean granitoids chiefly consist of tonalite-trondhjemite-granodiorite (TTG) gneisses and K-rich granitoids (Laurent et al., 2014). TTG gneisses dominate in the early Archean terranes, and are typically considered as partial melts derived from hydrous metabasalts at high pressures with a significant fraction of garnet in the residuum (Rapp et al., 2003; Moyen and Martin, 2012). Inferred tectonic settings for the TTG gneisses include subducted oceanic slabs or plateaus in a subduction-related environment (Xiong et al., 2009; Martin et al., 2014), and over-thickened mafic crust associated with mantle plumes (Smithies, 2000; Condie, 2005; Campbell and Davies, 2017). Towards the end of the Archean, the proportions of K-rich granitoids increase significantly, which constitute approximately 20% of the preserved Archean crust. Their presence heralds craton thickening and stabilization (Kumar et al., 2011; Romano et al., 2013). Although the late Archean K-rich granitoids were emplaced diachronously among cratons, they generally display intrusive contacts with supracrustal successions and TTG gneisses.

The K-rich granitoids can primarily be subdivided into sanukitoids and potassic granites according to their petrographic and geochemical characteristics. Sanukitoids, first proposed by Shirey and Hanson (1984) in Superior Province, have now been recognized from several Archean cratons (Martin et al., 2009; Mikkola et al., 2014; Semprich et al., 2015; Jiang et al., 2016). The compositions of sanukitoids vary from diorites and monzodiorites, corresponding to the original usage by Shirey and Hanson (1984), to granodiorites and granites (Heilimo et

al., 2010). All are characterized by high Mg# values (100Mg/(Mg+Fe_{total}), 45-65), Ni and Cr concentrations, as well as enriched LILEs and LREEs (Martin et al., 2009, 2014; Heilimo et al., 2010). The petrogenesis of Archean sanukitoids has been suggested by a single-stage model in which slab melt was contaminated by mantle peridotite, or a two-stage model in which metasomatism of the lithospheric mantle was followed by partial melting (Smithies and Champion, 2000; Heilimo et al., 2010; Semprich et al., 2015). The recognition of sanukitoids after 2.95 Ga, indicating the presence of enriched mantle sources, has led to discussions about their occurrence making the onset of plate tectonics (Heilimo et al., 2010; 2013; Chiaradia et al., 2014).

Archean potassic granites typically consist of granodiorites, monzogranites, and syenogranites, displaying high SiO_2, K_2O, and LILEs but low CaO, Fe_2O_3, MgO, and Cr contents, and are generally considered to form through melting of crustal lithologies (Frost et al., 2006; Kumar et al., 2011). They are generally emplaced shortly after sanukitoids, and commonly represent the last major Archean craton forming magmatic event. Potassic granites are commonly believed to have generated in extensional settings where enough external heat can be received through asthenosphere upwelling or magma underplating (Frost et al., 2006; Hinchey et al., 2011). Systematic studies of the sanukitoids and associated crust-derived potassic granites are important to evaluate the late Archean crustal evolution and crust-mantle interaction.

The Neoarchean granitoids in Western Liaoning Province of the northern North China Craton (NCC, Fig. 1A) primarily consist of K-rich granitoids in the southeast and TTG gneisses in the northwest (Fig. 1B; Wang et al., 2012, 2015, 2016; Zhang et al., 2016; Fu et al.,

2017; Liu et al., 2018). The K-rich granitoids contain minor xenoliths of TTG gneisses, and chiefly comprise porphyritic monzodioritic-quartz monzodioritic-granodioritic-monzogranitic (MQGM) gneisses and subordinate monzogranite-syenogranites (Fig. 1C). The porphyritic MQGM gneisses show geochemical affinities to either sanukitoids or potassic granites. In most Archean cratons in the world, sanukitoids and potassic granites are typically exposed as plutons or dykes intruded into the TTG gneisses (Heilimo et al., 2010; Laurent et al., 2014). However, in Western Liaoning Province, the sanukitoids and potassic granites in the southeast emplaced after their TTG xenoliths, but are coeval with, or even slightly earlier than the TTG gneisses to the northwest. This temporal overlap provides an opportunity to assess the petrogenetic relationships between TTG gneisses, sanukitoids, and potassic granites, as well as to speculate on the changing geodynamics at the end of the Archean.

In this contribution, we focus on the porphyritic MQGM gneisses and their TTG xenoliths, providing new field geological, petrological, in-situ zircon U-Pb chronological and Lu-Hf isotopic, and whole-rock geochemical data with the aims of: (1) establishing the Neoarchean lithological assemblages and geochronological framework of the Western Liaoning basement terranes; (2) deciphering the petrogenesis and tectonic environment of the MQGM gneisses and their TTG xenoliths; and (3) constraining the Neoarchean crust-mantle interaction and crustal evolution of the Western Liaoning Province in northern NCC.

2. Geological background

The Archean metamorphic basement of the NCC preserves rocks up to ca. 3.8 Ga, and is dominated by late Neoarchean lithological assemblages (Liu et al., 1992, 2004, 2011; Yang et

al., 2008; Nutman et al., 2011; Zhai et al., 2013; Bai et al., 2014, 2016; Guo et al., 2015, 2016, 2017; Fu et al., 2016; Wang et al., 2017). Zhao et al. (2005) proposed that the NCC metamorphic basement can be tectonically divided into the Archean Eastern and Western Blocks and the intervening Paleoproterozoic Trans-North China Orogen (Fig. 1A). Zhai and Santosh (2011) proposed that Archean NCC basement can be divided into the Jining, Jiaoliao, Qianhuai, Xuchang, Xuhuai, Alashan, and Ordos microblocks, and suggested that they were amalgamated along greenstone belts at ca. 2.5 Ga. Recently, Wang et al. (2015) suggested a late Neoarchean intra-oceanic arc system in the northwestern Eastern Block, which shows abundant ca. 2.6-2.5 Ga rocks but no involvement of older materials. The Western Liaoning basement terranes lie in the northern Eastern Block in the scenario of Zhao et al. (2005) (Fig. 1A), in the central Jining microblock in the scenario of Zhai and Santosh (2011), and in the middle segment of the late Neoarchean intra-oceanic arc and earlier continental basement in the scenario of Wang et al. (2015). Neoarchean lithological assemblages in the metamorphic terranes mainly consist of intrusive granitoid orthogneisses with blocks or enclaves of supracrustal rocks (Lin et al., 1992; Liu et al., 2010, 2011; Wang et al., 2012, 2015, 2016; Zhang et al., 2016; Fu et al., 2017). According to our field investigation, the basement terranes in the Western Liaoning Province can be divided into the northern zone, northwestern zone and southeastern zone (Fig. 1B).

The northern zone is distributed in the northern Fuxin area (Fig. 1B), and mainly consists of 2640-2603 Ma tholeiitic basalts and magnetite quartzites. The tholeiitic basalts are geochemically analogous to N-MORB or E-MORB, and were considered remnants of oceanic crusts that were derived from the melting of depleted or slightly enriched mantle sources

(Wang et al., 2011, 2015).

The northwestern zone is primarily distributed in the Jianping-Chaoyang-Fuxin areas (Fig. 1B), and separated from the northern zone by a ductile shear zone. The lithological assemblages in this zone are composed of 2589-2522 Ma supracrustal rocks, 2538-2506 Ma TTG gneisses, and minor 2496-2494 Ma weakly deformed potassic granites. The supracrustal succession is dominated by metamorphosed calc-alkaline basaltic-basaltic andesitic-andesitic rocks and tholeiitic basalts, and typically exposed as blocks or xenoliths within the granitoids. They are geochemically analogous to high magnesium andesites, adakites, boninites, and island arc tholeiites, and are therefore considered to be generated in arc-related settings (Wang et al., 2011, 2015). The TTG gneisses are the dominant Neoarchean lithological assemblages in this zone, and generally show intrusive contacts with the supracrustal succession. According to their geochemical affinities with adakites, sanukitoids, or melts derived from lower crust, these TTG gneisses were thought to be developed in a supra-subduction zone setting (Wang et al., 2012, 2013, 2015). The sporadic potassic granites expose as dykes within the TTG gneisses and supracrustal sequence, and were interpreted to be generated by metapelites melting (Wang et al., 2012, 2013).

The southeastern zone is mainly distributed in the Jinzhou-Xingcheng-Suizhong areas (Fig. 1B), and separated from the northwestern zone by large-scale nappe structures. The Neoarchean lithological assemblages in this zone predominantly consist of K-rich granitoids with minor TTG gneisses and supracrustal rocks. The TTG gneisses and supracrustal rocks were intruded by K-rich granitoids, and typically exposed as xenoliths within the granitoids (Fig. 2A and B). The K-rich granitoids are termed the Suizhong granitoids. Our geological

investigation suggests that the K-rich granitoids may be subdivided into porphyritic MQGM gneisses and medium-grained monzogranite-syenogranites according to their distinct lithological assemblages and deformation features (Fig. 1C). The MQGM gneisses are mostly strongly deformed and characterized by high mafic mineral contents and porphyritic textures, with K-feldspar as the dominant phenocrysts (Fig. 2). Based on their major mafic mineral phases, these porphyritic MQGM gneisses may be further divided into an amphibole-dominated group (ADG) and a biotite-dominated group (BDG). The ADG is chiefly composed of monzodioritic, quartz monzodioritic, granodioritic, and monzogranitic gneisses, and is characterized by amphibole as a major mafic mineral phase (Fig. 2B, C, and D). While the BDG mainly consists of granodioritic and monzogranitic gneisses, with a mafic mineral phase dominated by biotite (Fig. 2A, E, and F). The monzogranite-syenogranites are massive or weakly deformed and have low mafic mineral contents. They intruded the widespread MQGM gneisses and represent the last Archean magmatic episode in this region (Fig. 2F). Fu et al. (2017) argued that these 2527-2511 Ma monzogranite-syenogranites were generated in a back-arc basin setting by melting of the porphyritic MQGM gneisses at low pressure, and experienced fractionation of titanite, epidote, allanite, zircon and apatite during their magmatic evolution.

3. Petrology

We collected twenty-six representative samples from the southeastern zone, including one tonalitic gneiss xenolith, twelve ADG and thirteen BDG porphyritic MQGM gneisses. The tonalitic gneiss xenolith displays gneissic structure and fine-to medium-grained texture,

and chiefly comprises quartz (24%), K-feldspar (6%), plagioclase (54%), amphibole (3%), and biotite (13%) (Table 1; Fig. 3A), with accessory minerals of apatite, zircon, magnetite, and titanite. The K-feldspar mainly consists of anhedral orthoclase and perthite. The plagioclase is typically subhedral to anhedral, and has experienced low degrees of sericitization.

The porphyritic MQGM gneisses display gneissic structure and porphyritic texture, with K-feldspar the dominant phenocryst phase. The ADG samples comprise one monzodioritic, two quartz monzodioritic, four granodioritic, and five monzogranitic gneisses. They are mainly composed of quartz (4-23%), K-feldspar (15-27%), plagioclase (36-56%), amphibole (8-16%), and biotite (4-8%) (Table 1; Fig. 3B and C). The BDG samples comprise five granodioritic and eight monzogranitic gneisses, and primarily consist of quartz (21-26%), K-feldspar (19-29%), plagioclase (35-47%), amphibole (0-6%), and biotite (5-13%) (Table 1; Fig. 3D and E). In general, the ADG samples show higher mafic mineral contents (Amp+Bi, 14-23%) than the BDG samples (8-15%). Titanite, epidote, allanite, zircon, and apatite are the main accessory minerals in these porphyritic MQGM gneisses. The K-feldspar primarily consists of anhedral microcline, orthoclase, and perthite. The plagioclase generally occurs as euhedral to subhedral crystals, and experienced different degrees of saussuritization and sericitization. Amphibole and biotite have been partly altered to epidote and chlorite. Additionally, euhedral magmatic epidote, generally associated with and partially enclosed by amphibole and biotite, can also be identified in these MQGM gneisses (Fig. 3F). Allanite and titanite are commonly euhedral to subhedral, whereas apatite is generally anhedral.

4. Analytical methods

Whole-rock major and trace element contents of the twenty-six investigated samples were analyzed by X-ray Fluorescence (XRF) spectrometry and Agilent 7500 high-resolution ICP-MS, respectively. The analytical results and detailed procedures are presented in Appendix Table A1. Nine representative samples, including the tonalitic gneiss xenolith (15LX21-1), three ADG porphyritic MQGM gneisses (15LX01-2, 15LX19-2, and 15LX88-1), and five BDG porphyritic MQGM gneisses (15LX03-1, 15LX38-1, 15LX47-1, 15LX52-1, and 15LX54-1) were selected for in-situ zircon U-Pb chronological analyses by a laser ablation inductively coupled plasma mass spectrometer (LA-ICPMS), and for in-situ Lu-Hf isotopic analyses by a Neptune Plus MC-ICP-MS with an attached 193 nm laser ablation system. The analytical results and detailed procedures are given in Appendix Table A2 and A3.

5. Analytical results

5.1. Whole-rock Geochemistry

5.1.1. The Tonalitic Gneiss Xenolith

The analyzed sample, 15LX21-1, is a tonalitic gneiss xenolith in a porphyritic monzogranitic gneiss (Fig. 4A). It displays high SiO_2 (69.28 wt.%), MgO (1.70 wt.%), CaO (3.39 wt.%), and Fe_2O_3 (4.29 wt.%) contents, but low K_2O content (1.60 wt.%), with a higher Mg# value ($100Mg/(Mg+Fe_{total})$, 43.95) but a lower K_2O/Na_2O ratio (0.47). In the total alkali versus silica (TAS) classification diagram (Fig. 4B) it falls in the granodiorite range, and in the K_2O versus SiO_2 diagram it falls in the bottom of the medium-K calc-alkaline series (Fig.

4C). In the MgO versus SiO_2 diagram, this sample plots within the high-silica adakite (HSA) range, with MgO content and Mg# value higher than those of the experimental partial melts from basalt (PMB) (Fig. 4D and E). This sample also exhibits peraluminous character due to high A/CNK (molar $Al_2O_3/(CaO+Na_2O+K_2O)$) value of 1.10 (Fig. 4F).

This tonalitic gneiss sample shows strongly fractionated chondrite-normalized REE pattern with a high $(La/Yb)_N$ ratio of 42, and slightly positive Eu anomaly ($Eu_N/Eu_N^* = 1.09$) (Fig. 5A). In the primitive mantle (PM)-normalized spider diagram, this sample shows negative Ba, Ti, Nb, Ta, and P anomalies and positive Rb, K, Hf, and Zr anomalies (Fig. 5B).

5.1.2. The Amphibole-dominated Group (ADG)

The twelve analyzed ADG samples display low SiO_2 (54.32-66.15 wt.%), but high MgO (1.78-4.14 wt.%) contents, and fall within the fields of monzodiorite, monzonite, quartz monzonite, granodiorite in the TAS classification diagram (Fig. 4B). These samples show high K_2O contents of 2.44-4.50 wt.%, and plot in the ranges of high-K calc-alkaline and shoshonite series (Fig. 4C). Among them, six samples display higher MgO contents than the PMB, whereas the remaining six plot within the upper range of the PMB field (Fig. 4D). Most samples display high Mg# values (46.75-51.03) and plot above the PMB field, except for sample 15LX88-1, which shows a slightly lower Mg# value of 41.10 and falls within the PMB field (Fig. 4E). These ADG samples also have Al_2O_3, CaO, and Na_2O contents of 14.69-17.91 wt.%, 3.01-6.30 wt.%, and 2.48-3.86 wt.% (Table A1), respectively, resulting in A/CNK values of 0.88-1.09 and ranging from metaluminous to peraluminous (Fig. 4F).

The ADG samples show flat to moderately fractionated REE patterns, with $(La/Yb)_N$

ratios varying from 5.68 to 27, and slightly negative to positive Eu anomalies, with Eu_N/Eu_N* values ranging from 0.62 to 1.17 (Table A1 and Fig. 5A). They are enriched in LREEs and LREEs, but depleted in Ta, Ti, and Nb in the PM-normalized spider diagram (Fig. 5B).

5.1.3. The Biotite-dominated Group (BDG)

Compared with the ADG samples, the thirteen analyzed BDG samples generally exhibit higher SiO_2 (63.27-71.70 wt.%), but lower MgO (1.08-2.01 wt.%) and CaO (2.05-3.32 wt.%) contents, and mostly plot within the granodiorite and granite fields in both the An-Ab-Or and TAS diagrams (Fig. 4A and B). The MgO and K_2O (3.05-4.50 wt.%) contents of these samples show quite limited variations, and all samples from this group are attributed to the high-K calc-alkaline series (Fig. 4C) and fall within the PMB range in the MgO versus SiO_2 diagram (Fig. 4D). Besides, most samples have lower Mg# values of 35.37-45.93 and fall within the PMB field, except for sample 15LX21-3, which has a much higher Mg# value of 49.61 (Fig. 4E). They are all peraluminous with high A/CNK values between 1.02 and 1.15 (Fig. 4F).

These BDG samples are characterized by moderately to highly fractionated REE patterns, with $(La/Yb)_N$ ratios between 17.8 and 41, and slightly negative to positive Eu anomalies (Eu_N/Eu_N* = 0.81-1.56) (Table A1 and Fig. 5C). In the PM-normalized spider diagram, they are enriched in LILEs, LREEs, Zr, and Hf, but depleted in Ta, Nb, P, and Ti (Fig. 5D).

5.2. Zircon Geochronology and Lu-Hf Isotopes

Zircon grains from the nine dated samples generally have prismatic to elliptical shapes,

with lengths of 100-400 um and length/width ratios 3:1-1:1 (Fig. 6). Zircon grains separated from the tonalitic gneiss xenolith 15LX21-1 show complicated core-mantle-rim internal structures, with blurred oscillatory zoned cores encircled by dark structureless mantles and bright structureless rims (Fig. 6A). Zircons from the quartz monzodioritic gneiss 15LX19-2 and the granodioritic gneisses 15LX01-2 and 15LX03-1 typically show core-rim structures, with blurred oscillatory zoned or structureless cores enveloped by structureless rims (Fig. 6B, C, and E). Whereas zircons grains from the granodioritic gneisses 15LX88-1, 15LX47-1, and 15LX52-1 and the monzogranitic gneisses 15LX38-1 and 15LX54-1 typically exhibit clear oscillatory zoning with some grains suffering various degrees of metamictization (Fig. 6D, F, G, H, and I).

5.2.1. The Tonalitic Gneiss Xenolith

Thirty zircon spots from the tonalitic gneiss xenolith 15LX21-1 were analyzed for U-Pb isotopes, and twenty-six of which are concordant with apparent $^{207}Pb/^{206}Pb$ ages ranging from 2695 ± 15 Ma to 2495 ± 15 Ma (Table A2). Spot #29 was conducted on a structureless core, yielding an oldest $^{207}Pb/^{206}Pb$ age of 2695 ± 15 Ma and a high Th/U ratio of 0.66. This age is much older than the other analyses and the formation ages of the regional supracrustal succession (2640-2522 Ma; Wang et al., 2011, 2015), and is therefore considered as inherited zircon from either the country rocks or source region. Thirteen analyses on cores have similar $^{207}Pb/^{206}Pb$ ages between 2578 ± 15 Ma and 2549 ± 16 Ma and high Th/U ratios of 0.74-2.04, defining a weighted mean age of 2563 ± 6 Ma (MSWD = 1.6, Fig. 7A). According to the oscillatory zoning (Fig. 6A) and high Th/U ratios, this age (2563 ± 6 Ma) is regarded as the

magmatic emplacement age of this tonalitic gneiss. The other twelve concordant analyses were performed on mantles and rims, and have much younger $^{207}Pb/^{206}Pb$ ages from 2516 ± 15 Ma to 2495 ± 15 Ma with Th/U ratios of 0.83-0.02, giving a weighted mean age of 2506 ± 4 Ma (MSWD = 0.8, Fig. 7A), which is younger than the emplacement ages of the regional Neoarchean granitoids in the southeastern zone. Considering the internal structures and lower Th/U ratios as well as the geological relationship as a tonalitic gneiss xenolith in the K-rich granitoids, these younger ages may be interpreted as metamorphic records.

Fifteen dated spots from sample 15LX21-1 were analyzed for in-situ Lu-Hf isotopes (Table A3). Spot #29 from the inherited zircon grain displays a $\varepsilon Hf(t_1)$ value of +5.4. The remaining fourteen analyses are corrected to their emplacement age (t_2) and show positive $\varepsilon Hf(t_2)$ values between +3.1 and +5.9 (Fig. 8A).

5.2.2. The Amphibole-dominated Group (ADG)

Thirty spots from the granodioritic gneiss sample 15LX01-2 were analyzed for U-Pb isotopes, and twenty-five of which are concordant with apparent $^{207}Pb/^{206}Pb$ ages from 2548 ± 16 Ma to 2500 ± 16 Ma. Among them, sixteen analyses from oscillatory zoned cores show apparent $^{207}Pb/^{206}Pb$ ages between 2548 ± 16 Ma and 2522 ± 16 Ma with Th/U ratios of 2.04-0.34, providing a weighted mean $^{207}Pb/^{206}Pb$ age of 2535 ± 5 Ma (MSWD = 1.4). Considering their oscillatory zoning (Fig. 6B) and high Th/U ratios, the age of 2535 ± 5 Ma is taken as the magmatic crystallization age of this granodioritic gneiss. The other nine concordant analyses were mainly performed on rims, and show younger apparent $^{207}Pb/^{206}Pb$ ages from 2517 ± 16 Ma to 2500 ± 16 Ma and Th/U ratios of 1.30-0.24 (Fig. 7B). According

to their internal structures and lower Th/U ratios, these younger ages is attributed to either regional metamorphic events or the effects of emplacement event of the 2527-2511 Ma monzogranite-syenogranites. Sixteen Lu-Hf isotopic analyses for sample 15LX01-2 are calculated back to the crystallization age (t_2), and display positive $\varepsilon Hf(t_2)$ values from +2.9 to +7.2 (Fig. 8B).

Thirty spots from the quartz monzodioritic gneiss sample 15LX19-2 were analyzed for U-Pb isotopes, and twenty-six of which plot on concordia with apparent $^{207}Pb/^{206}Pb$ ages from 2543 ± 14 Ma to 2496 ± 14 Ma. Eighteen analyses on blurred oscillatory zoned cores exhibit similar apparent $^{207}Pb/^{206}Pb$ ages from 2543 ± 14 Ma to 2518 ± 14 Ma and Th/U ratios of 1.03-0.61, and define a weighted mean age of 2529 ± 4 Ma (MSWD = 1.2, Fig. 7C). Based on their oscillatory zoning (Fig. 6C) and high Th/U ratios of typical magmatic zircons, this age (2529 ± 4 Ma) is considered the magmatic emplacement age of this quartz monzodioritic gneiss. The other eight concordant analyses on rims show much younger apparent $^{207}Pb/^{206}Pb$ ages from 2510 ± 14 Ma to 2496 ± 14 Ma and Th/U ratios of 1.10-0.20. Considering their inner structures, these younger ages may be considered the records of later regional tectono-thermal events. Seventeen Lu-Hf isotopic analyses from sample 15LX19-2 are corrected back to the crystallization age (t_2), and display positive $\varepsilon Hf(t_2)$ values between +3.4 and +5.6 (Fig. 8C).

Thirty spots from the granodioritic gneiss sample 15LX88-1 were analyzed for U-Pb isotopes, and only seventeen are concordant or near-concordant. Most of these seventeen analyses were conducted on oscillatory zoned zircons, and display similar apparent $^{207}Pb/^{206}Pb$ ages between 2553 ± 15 Ma and 2542 ± 15 Ma and Th/U ratios of 0.93-0.36,

providing a weighted mean age of 2546 ± 4 Ma (MSWD = 0.13, Fig. 7D). Given their oscillatory zoning (Fig. 6D) and high Th/U ratios, the age of 2546 ± 4 Ma is regarded as the magmatic emplacement age of sample 15LX88-1. Sixteen Lu-Hf isotopic analyses from this sample are calculated back to their emplacement age (t_2), yielding positive εHf(t_2) values between +3.3 and +5.2 (Fig. 8D).

5.2.3. The Biotite-dominated Group (BDG)

Thirty spots from the granodioritic gneiss sample 15LX03-1 were analyzed for U-Pb isotopes, and twenty-seven of which plot on concordia with apparent $^{207}Pb/^{206}Pb$ ages from 2542 ± 15 Ma to 2512 ± 15 Ma. Among them, twenty-two analyses on cores show similar $^{207}Pb/^{206}Pb$ ages between 2542 ± 15 Ma and 2525 ± 15 Ma and Th/U ratios of 0.93-0.34, giving a weighted mean age of 2531 ± 3 Ma (MSWD = 0.36). Considering the oscillatory zoning (Fig. 6E) and high Th/U ratios, this age (2531 ± 3 Ma) is regarded as the magmatic emplacement age of this sample. The other five concordant analyses were performed on structureless rims or domains (Fig. 6E), and show younger apparent $^{207}Pb/^{206}Pb$ ages from 2524 ± 16 Ma to 2512 ± 15 Ma and Th/U ratios between 0.78 and 0.46, giving a weighted mean age of 2521 ± 7 Ma (MSWD = 0.46, Fig. 7E). The structures of these analytical zircon grains imply that these younger ages may reflect the effects of regional thermal events or the emplacement of the monzogranite-syenogranites. Seventeen Lu-Hf isotopic analyses from sample 15LX03-1 are corrected back their emplacement age (t_2), and display positive εHf(t_2) values between +2.7 and +6.0 (Fig. 8E).

A total of thirty spots from the monzogranitic gneiss sample 15LX38-1 were analyzed

for U-Pb isotopes, and only eight of them have concordant ages and plot along concordia. Among them, seven analyses on oscillatory zoned zircons have apparent $^{207}Pb/^{206}Pb$ ages between 2555 ± 15 Ma and 2536 ± 16 Ma with Th/U values between 0.85 and 0.39, and yield a weighted mean age of 2546 ± 6 Ma (MSWD = 1.00, Fig. 7F). According to their oscillatory zoning (Fig. 6F) and high Th/U ratios, this age is considered the magmatic emplacement age of this sample. The remaining concordant analysis was carried out on a blurred oscillatory zoned domain and yields a much younger apparent $^{207}Pb/^{206}Pb$ age of 2499 ± 69 Ma and Th/U ratio of 1.00, which may reflect the effects of regional tectono-thermal event. Sixteen Lu-Hf isotopic analyses from sample 15LX38-1 are calculated to their emplacement age (t_2), and most show positive $\varepsilon Hf(t_2)$ values from +0.46 to +2.72, except for spot #13, which has a negative $\varepsilon Hf(t_2)$ value of -1.8 (Fig. 8F).

Thirty spots from the granodioritic gneiss sample 15LX47-1 were analyzed for U-Pb isotopes, and most have subjected to strong lead loss. Only three analyses (spots #06, #13, and #24) are concordant with $^{207}Pb/^{206}Pb$ ages between 2554 ± 17 Ma and 2535 ± 19 Ma and high Th/U ratios from 1.30 to 0.79, and give a weighted mean age of 2544 ± 10 Ma (MSWD = 1.16, Fig. 7G). Based on their oscillatory zoning (Fig. 6G) and high Th/U ratios, this age is considered the magmatic emplacement age of this sample. Fourteen Lu-Hf isotopic analyses from sample 15LX47-1 are calculated back to their emplacement age (t_2), and have positive $\varepsilon Hf(t_2)$ values from +0.2 to +3.6 (Fig. 8G).

Thirty spots from the granodioritic gneiss sample 15LX52-1 were analyzed for U-Pb isotopes, however, most have experienced significant lead loss and plot under concordia. Only four analyses (spots #09, #24, #25, and #28) plot on concordia. Among them, spot #09, which

was performed on an oscillatory zoned zircon with a rounded shape, yields the oldest apparent $^{207}Pb/^{206}Pb$ age of 2577 ± 15 Ma and highest Th/U ratio of 0.77, which is much older than the other three concordant analyses, and consistent with the apparent $^{207}Pb/^{206}Pb$ ages of the magmatic zircons (2578-2549 Ma) from the tonalitic gneiss xenolith 15LX21-1. According to the intrusive relationship between the porphyritic MQGM gneisses and the TTG xenoliths (Fig. 2A), we suggest that this zircon may represent an inherited grain from either the country rocks or source region. The remaining three concordant analyses (spots #24, #25, and #28) on oscillatory zoned domains display slightly younger apparent $^{207}Pb/^{206}Pb$ ages from 2546 ± 15 Ma to 2539 ± 16 Ma and Th/U ratios between 0.40 and 0.35, and provide a weighted mean age of 2543 ± 9 Ma (MSWD = 0.21, Fig. 7H). Given their oscillatory zoning (Fig. 6H) and high Th/U ratios, the age of 2543 ± 9 Ma is regarded as the magmatic emplacement age of this sample. Sixteen dated zircon spots from sample 15LX52-1 were analyzed for Lu-Hf isotopes. Spot #09 from the inherited zircon show $\varepsilon Hf(t_1)$ value of +3.3. The other fifteen analyses are corrected to the emplacement age (t_2), and show positive $\varepsilon Hf(t_2)$ values between +1.6 and +4.4 (Fig. 8H).

Thirty spots from the monzogranitic gneiss sample 15LX54-1 were analyzed for U-Pb isotopes, and most have experienced significant lead loss with only ten analyses are concordant. Of which, eight analyses on oscillatory zoned zircons display similar apparent $^{207}Pb/^{206}Pb$ ages between 2549 ± 17 Ma and 2540 ± 17 Ma and Th/U ratios of 0.80-0.55, giving a weighted mean age of 2544 ± 6 Ma (MSWD = 0.14). Based on the oscillatory zoning (Fig. 6I) and high Th/U ratios, this age is considered the magmatic emplacement age of this sample. The remaining two concordant analyses (spots #19 and #23) were conducted on

blurred zoned domains, and exhibit much younger apparent $^{207}Pb/^{206}Pb$ ages between 2521 ± 17 Ma and 2450 ± 70 Ma (Fig. 7I). They may reflect the effects of regional thermal events or the emplacement of the monzogranite-syenogranites. Ten Lu-Hf isotopic analyses from sample 15LX54-1 are corrected to the emplacement age (t_2), and have positive εHf(t_2) values between +2.2 and +6.6 (Fig. 8I).

6. Discussion

6.1. Petrogenesis

6.1.1. The Tonalitic Gneiss Xenolith

TTG gneisses in the southeastern zone only occur as xenoliths in the K-rich granitoids, and zircon U-Pb dating reveals their crystallization age of 2563 ± 6 Ma. This contrasts with the northwestern zone where the TTG gneisses act as the dominant lithological assemblages and yield much younger crystallization ages of 2538-2506 Ma (Wang et al., 2012, 2013). The analyzed sample 15LX21-1 is characterized by high Na_2O, LREEs, and LILEs, but low K_2O, HREEs, Ti, Nb, and Ta contents, which are all typical geochemical features of the Archean TTG series (Fig. 4A, 9A and B), and similar to those of the Phanerozoic high-SiO_2 adakites (HSA; Fig. 4D). In both the MgO versus SiO_2 and Mg# versus SiO_2 diagrams (Fig. 4D and E), it exhibits MgO content and Mg# value higher than the experimental melts derived from basaltic rocks (PMB), indicating that the mantle materials have been involved into its melt. However, the high SiO_2 (69.28 wt.%) and low TiO_2 (0.56 wt.%) of this sample are inconsistent with its generation directly from melting of enriched or depleted mantle peridotite (Martin et al., 2009). Integrated with the narrowly positive zircon εHf(t_2) values of

this sample from +3.1 to +5.9 (Fig. 8A), a magma mixing between the mantle- and crust-derived melts has been excluded. Therefore, we consider that the magmatic precursor of the tonalitic gneiss xenolith was most likely generated by partial melting of subducted slabs, and the melt was contaminated by the mantle peridotite in its ascent process.

6.1.2. The Amphibole-dominated Group (ADG)

The analyzed ADG samples show high MgO (1.78-4.14 wt.%) and CaO (3.01-6.30 wt.%) contents, and Mg# values (41.10-51.03). Most samples display MgO contents and Mg# values higher than those of the experimental partial melts derived from basaltic rocks (Fig. 4D and E), excluding their derivation from pure crustal materials, and indicating mantle contribution to their generation. They also show high K_2O and LILEs (such as Ba, Sr, and Rb) contents as well as high K_2O/Na_2O ratios (Table A1). In this case, these geochemical features cannot be attributed to crystal fractionation, magma mixing or assimilation of felsic crust, because: (1) Archean crust generally displays lower contents of these elements, especially for K_2O; (2) these incompatible elements exhibit negligible changes across the range of silica contents; (3) the analyzed ADG samples define partial melting trends in the discrimination diagrams of La/Sm versus La and Cs/Sm versus Cs (Fig. 9D and E), indicating that their geochemical variations are primarily controlled by partial melting rather than magma mixing or crystal fractionation (Schiano et al., 2010); and (4) the dated samples from the ADG show limited variation in their $\varepsilon Hf(t_2)$ values (Fig. 8B, C, and D), together with the absence of inherited zircons, suggesting negligible effects of magma mixing and assimilation of felsic crust. Such geochemical signatures are similar to those of the typical Archean K-rich, Mg-rich

sanukitoids (Stern and Hanson, 1991; Smithies et al., 2007). In the K_2O versus SiO_2 and MgO versus SiO_2 diagrams (Fig. 4C and D), all the ADG samples fall within the fields of sanukitoids (Martin et al., 2009). In addition, the analyzed ADG samples exhibit high CaO (3.01-6.30 wt.%), Fe_2O_3 (3.60-8.94 wt.%), Sr (202-877 ppm), Ba (479-1531 ppm), Cr (26-238 ppm), and Ni (9.12-75 ppm) contents, as well as high K_2O/Na_2O (0.87-1.56) and $(La/Yb)_N$ (5.68-27) ratios, which are all comparable to those of the Archean sanukitoids from the Western Karelian Province in Finland (CaO, 0.87-8.11 wt.%; Fe_2O_3, 2.18-9.21 wt.%; Sr, 219-1320 ppm; Ba, 316-2896 ppm; Cr, 10-626 ppm; Ni, 10-221 ppm; K_2O/Na_2O, 0.33-2; $(La/Yb)_N$, 5.24-120; Heilimo et al., 2010). In the Na_2O+K_2O-CaO versus SiO_2, Na_2O/K_2O-2*A/CNK-2*FMSB ($(FeO_t+MgO)_{wt.\%}$*$(Sr+Ba)_{wt.\%}$), and FeO_t+MgO+MnO+TiO_2 versus SiO_2 diagrams, almost all of the ADG samples plot in the fields of sanukitoids (Fig. 9A, B, and C). Therefore, we propose these ADG samples as sanukitoids.

The younger emplacement ages (2546-2529 Ma) and significantly higher K_2O contents (2.44-4.50 wt.%) of the ADG samples than those of the tonalitic gneiss (2563 Ma and 1.60 wt.%, respectively), argue against their generation involving a single stage model in which slab melts assimilated mantle peridotites. Archean sanukitoids are commonly considered to be generated by the partial melting of a metasomatized mantle wedge (Martin et al., 2005; Rapp et al., 2010; Laurent et al., 2011, 2014; Mikkola et al., 2014). However, the metasomatic agents that lead to the enrichment of LILEs in the mantle wedge are uncertain and include: (1) partial melts derived from descending oceanic slabs (Smithies and Champion, 2000; Martin et al., 2009; Rapp et al., 2010); (2) partial melts of the subducted sedimentary rocks (Laurent et al., 2011; Fowler and Rollinson, 2012); (3) slab- or sedimentary-derived dehydration fluids

(Wang et al., 2009; Jiang et al., 2016); and (4) alkaline melts/fluids from the upwelling asthenosphere (Lobach-Zhuchenko et al., 2008; de Oliveira et al., 2010, 2011; Semprich et al., 2015).

The temporal relationships between the ADG samples and the TTG gneiss xenoliths, integrated with the petrogenesis of the tonalitic xenolith stated above, suggest that slab melts are an important metasomatic agent for the mantle source of the ADG samples. Whereas slab melts that are derived from oceanic crusts (MORB) may be negligible for K and LILE enrichments (Lobach-Zhuchenko et al., 2008), therefore, are impossible to be the only agent of mantle metasomatism. The dated ADG samples (15LX01-2, 15LX19-2, and 15LX88-1) show zircon εHf(t_2) values significantly lower than the contemporaneous depleted mantle (Fig. 8B, C, and D), together with the peraluminous and high K_2O features of most ADG samples (Fig. 4C and F), suggesting that melts derived from sedimentary rocks should be a crucial metasomatic agent for the mantle source of the ADG samples. Moreover, the large variations of $(Hf/Sm)_N$ (1.38-0.22) and $(Nb/La)_N$ (0.59-0.14) ratios in these ADG samples suggest that dehydration fluids may also be an important metasomatic agent (Fig. 9F; LaFlèche et al., 1998). Therefore, the sanukitoid melts of the ADG porphyritic MQGM gneisses were most likely generated by partial melting of lithospheric mantle that was metasomatized by dehydration fluids and melts derived from subducted oceanic sediments and slabs. Geochemical variations within the ADG samples likely reflect variations in degrees of metasomatism or partial melting of the mantle source.

6.1.3. The Biotite-dominated Group (BDG)

The analyzed BDG samples exhibit low MgO (1.08-2.01 wt.%) and CaO (2.05-3.32 wt.%) contents, and plot within the PMB range in the MgO versus SiO_2 diagram (Fig. 4D), indicating a crustal source. Moreover, most of these samples exhibit low Mg# values of 35.37-45.93 and fall within the PMB field in the Mg# versus SiO_2 diagram, except for sample 15LX21-3 showing a much higher Mg# value of 49.61 due to lower Fe_2O_3 content, and plots above the PMB field (Fig. 4E). In the AFM (molar $Al_2O_3/(MgO+FeO_t)$) versus CFM (molar $CaO/(MgO+FeO_t)$) diagram, these BDG samples display high CFM but low AFM values (Table A1 and Fig. 9G), together with their low MgO contents and Mg# values, implying that their magmatic precursors were formed by the melting of basaltic sources. They show significantly higher K_2O contents (3.05-4.50 wt.%) than those of the experimental partial melts from low-K mafic sources (0.01-2.58 wt.% at SiO_2 contents of 60-75 wt.%; Beard and Lofgren, 1989, 1991; Rapp and Watson, 1995; Qian and Hermann, 2013), but within the range of the experimental melts derived from medium- to high-K basalt-basaltic andesite (2.94-5.94 wt.% at SiO_2 contents of 60-75 wt.%) reported by Sisson et al. (2005). Furthermore, in the $3*CaO-Al_2O_3/(FeO_t+MgO)-5*K_2O/Na_2O$ ternary diagram (Fig. 9H), almost all of the BDG samples plot within the melt composition range derived from high-K mafic rocks. As suggested by Sisson et al. (2005), medium- to high-K basalt-andesites are widespread and abundant in modern subduction zones. Fresh metavolcanic rocks in the northwestern zone that are contemporaneous with the BDG show SiO_2 and K_2O contents of 44.34-63.78 wt.% and 0.10-3.48 wt.%, respectively, and are mainly medium-K to high-K calc-alkaline series. These metavolcanic rocks typically display low LOI values and absence of Ce anomalies, indicating the general preservation of their original chemical features (Wang et al., 2011, 2015).

Therefore, we suggest that the BDG samples were generated by the partial melting of medium- to high-K mafic rocks.

In the La/Sm versus La and Cs/Sm versus Cs diagrams, the BDG samples define a partial melting trend, indicating that their geochemical variations are chiefly determined by a partial melting process (Fig. 9D and E). The BDG samples exhibit moderately to highly fractionated and concave upward chondrite-normalized REE patterns and weakly negative to positive Eu anomalies (Fig. 5C). These features, together with the slightly negative to positive Sr anomalies (δSr = 0.93-1.61) in the PM-normalized spider diagram (Fig. 5D), indicate that the BDG samples were mainly derived from the partial melting of medium- to high-K mafic rocks at medium pressures with garnet, plagioclase, and amphibole as the main residual phases.

6.2. Implications for Neoarchean Tectonic Setting and crustal Evolution of the Western Liaoning basement terranes

The Neoarchean lithological assemblages in the Western Liaoning basement terranes display characteristic zonation, with 2640-2603 Ma tholeiitic basalts dominated in the northern zone, 2589-2522 Ma metavolcanic rocks and 2538-2506 Ma TTG gneisses dominated in the northwestern zone, and 2546-2511 Ma K-rich granitoids dominated in the southeastern zone (Fig. 1B and 10; Liu et al., 2011, 2018; Wang et al., 2011, 2012, 2013, 2015, 2016; Zhang et al., 2016; Fu et al., 2017). The 2640-2603 Ma tholeiitic basalts in the northern zone represent the oldest exposed rocks in the Western Liaoning basement terranes of the NCC, and show geochemical affinities to N-MORB or E-MORB (Wang et al., 2011, 2015).

Wang et al. (2015) proposed that they may represent remnants of oceanic crust. The 2589-2522 Ma metavolcanic rocks in the northwestern zone display geochemical affinities to island arc tholeiites (IATs), calc-alkaline basalts (CABs), adakites, or high magnesium andesites. Petrogenetic studies have revealed that they were generated by partial melting of lithospheric mantle metasomatized by slab-derived fluids or melts, or by melting of subducted oceanic slabs (Wang et al., 2011, 2015). The 2538-2506 Ma TTG gneisses in the northwestern zone were suggested to be generated by partial melting of subducted oceanic slabs or basaltic lower crust (Wang et al., 2012, 2013). Based on the formation of island arc tholeiites (IATs) and absence of ≥ 2.7 Ga geological records, Wang et al. (2015) proposed that the Neoarchean lithological assemblages in the northwestern zone were generated under an intra-oceanic arc setting.

As discussed above the petrogenesis section, the ～2563 Ma TTG xenoliths and 2546-2529 Ma ADG porphyritic MQGM gneisses in the southeastern zone also indicate a subduction-related setting. Whereas the distinct Neoarchean lithological assemblages in the southeastern and northwestern zones suggest that they were generated under different geodynamic settings. In the southern Jinzhou area, a Mesozoic mafic dyke (100 ± 1 Ma) intruding the porphyritic MQGM gneisses contains early Mesoarchean captured zircons with apparent $^{207}Pb/^{206}Pb$ ages from 3140 ± 15 to 3041 ± 15 Ma (see Appendix Table A4 for details). These early Mesoarchean captured zircons, together with the ～ 2695 Ma inherited zircon from the tonalitic gneiss sample 15LX21-1 (Fig. 7A), suggest the existence of paleo-continental materials in the southeastern zone, integrating with the ca. 3.5-3.4 Ga supracrustal rocks and 3.3-2.9 Ga tonalitic-trondhjemitic gneisses in the Caozhuang area

(Nutman et al., 2011; Han et al., 2014; and our unpublished data) and the ca. 2.9 Ga metavolcanic rocks and TTG gneisses in the Caochang area (Liou et al., 2017) of the Eastern Hebei Province, indicating that the Neoarchean lithological assemblages in the southeastern zone were most likely developed in a tectonic setting of active continental margin. The terrigenous sediments from the paleo-continental block recycled into the mantle along with the subduction of oceanic slab, which may be a main source of K in the sanukitoids.

The Neoarchean lithological assemblages in the southeastern zone may be generated by the following processes: (1) subduction of oceanic slabs beneath the paleo-continent block started before ～2.56 Ga, and the partial melts from subducted slabs ascended through and interacted with the mantle wedge, resulting in the generation of the ～2563 Ma TTG gneiss xenoliths (Fig. 11); (2) with continuous subduction, the metasomatism of lithospheric mantle was enhenced by dehydration fluids and melts derived from subducted oceanic sediments and slabs. During 2.55-2.53 Ga, the partial melting of the progressively metasomatized lithospheric mantle led to the generation of the 2546-2529 Ma ADG porphyritic gneisses (sanukitoids). At the same time, the accompanied high geothermal gradients triggered the melting of medium-K to high-K mafic rocks at medium pressures, resulting in the formation of the 2546-2531 Ma BDG porphyritic MQGM gneisses (Fig. 11); and (3) during 2.53-2.51 Ga, the southeastern zone evolved under a back-arc basin setting, and the accompanied high geothermal gradients and decompression triggered the melting of porphyritic MQGM gneisses, giving rise to the 2527-2511 Ma monzogranite-syenogranites (Fu et al., 2017; Fig. 11).

7. Conclusions

(1) The porphyritic MQGM gneisses and the tonalitic gneiss xenolith in the southeastern zone of Western Liaoning basement terranes of the NCC were emplaced during 2546-2529 Ma and at 2563 Ma, respectively.

(2) The magma of the tonalitic gneiss xenolith was likely derived from partial melting of subducted oceanic slabs, with the melt contaminated by the mantle peridotite during its ascent. The porphyritic MQGM gneisses can be divided into an amphibole-dominated group (ADG) and a biotite-dominated group (BDG). The ADG porphyritic MQGM gneisses are geochemically analogous to sanukitoids, and their magmatic precursors were formed by partial melting of lithospheric mantle that was metasomatized by dehydration fluids and melts derived from subducted oceanic sediments and slabs. The magmas of the BDG porphyritic MQGM gneisses originated from partial melting of medium-K to high-K mafic rocks at medium pressures.

(3) The Neoarchean lithological assemblages in the southeastern zones of the Western Liaoning Province were most likely formed in a tectonic setting of active continental margin.

Acknowledgments

We are grateful to Editor Xianhua Li and the two anonymous reviewers for their thoughtful and constructive reviews, which greatly improved the quality of this manuscript. We also wish to thank Bin Yang, Fang Ma, and Libing Gu for their assistance in the whole-rock geochemical and LA-ICP-MS zircon U-Pb isotopic analyses, and Zhaochu Hu for the MC-ICP-MS zircon Lu–Hf isotopic analyses. This study is financially supported by the

National Natural Science Foundation of China (Grant Nos. 41530207, 41772188 and 41472165). Peter A. Cawood acknowledges support from Australian Research Council grant FL 160100168.

References

Altherr, R., Holl, A., Hegner, E., 2000. High-potassium, calc-alkaline I-type plutonism in the European Variscides: Northern Vosges (France) and northern Schwarzwald (Germany). Lithos 50, 51–73.

Bai, X., Liu, S.W., Guo, R.R., Zhang, L.F., Wang, W., 2014. Zircon U-Pb–Hf isotopes and geochemistry of Neoarchean dioritic–trondhjemitic gneisses, Eastern Hebei, North China Craton: constraints on petrogenesis and tectonic implications. Precambrian Research 251, 1–20.

Bai, X., Liu, S.W., Guo, R.R., Wang, W., 2016. A Neoarchean arc-back-arc system in Eastern Hebei, North China Craton: constraints from zircon U-Pb–Hf isotopes and geochemistry of dioritic–tonalitic–trondhjemitic–granodioritic (DTTG) gneisses and felsic paragneisses. Precambrian Research 273, 90–111.

Barker, F., 1979. Trondhjemite: definition, environment and hypotheses of origin. In: Barker, F. (Ed.), Trondhjemites, Dacites, and Related Rocks. Elsevier, Amsterdam, pp. 1–12.

Beard, J.S., Lofgren, G.E., 1989. Effect of water on the composition of partial melts of greenstone and amphibolite. Science 244, 195–197.

Beard, J.S., Lofgren, G.E., 1991. Dehydration melting and water-saturated melting of basaltic and andesitic greenstones and amphibolites at 1, 3, and 6.9 kb. Journal of Petrology 32, 365–401.

Blichert-Toft, J., Albarède, F., 1997. The Lu–Hf geochemistry of chondrites and the evolution of the mantle–crust system. Earth and Planetary Science Letters 148, 243–258.

Campbell, I.H., Davies, D.R., 2017. Raising the continental crust. Earth and Planetary Science Letters 460, 112-122.

Chiaradia, M., Muntener, O., Beate, B., 2014. Quaternary sanukitoid-like andesites generated by intracrustal processes (Chacana Caldera Complex, Ecuador): implications for Archean sanukitoids. Journal of Petrology 55, 769–802.

Condie, K.C., 2005. High field strength element ratios in Archean basalts: a window to evolving sources of mantle plumes? Lithos 79, 491–504.

de Oliveira, M.A., Dall'Agnol, R., Scaillet, B., 2010. Petrological constraints on crystallization conditions of Mesoarchean sanukitoid rocks, Southeastern Amazonian Craton, Brazil. Journal of Petrology 51, 2121–2148.

de Oliveira, M.A., Dall'Agnol, R., Almeida, J.d.A.C.d., 2011. Petrology of the Mesoarchean Rio Maria suite and the discrimination of sanukitoid series. Lithos 127, 192–209.

Fowler, M., Rollinson, H., 2012. Phanerozoic sanukitoids from Caledonian Scotland: implications for Archean subduction. Geology 40, 1079–1082.

Frost, C.D., Frost, B.R., Kirkwood, R., Chamberlain, K.R., 2006. The tonalite–trondhjemite–granodiorite (TTG) to granodiorite–granite (GG) transition in the late Archean plutonic rocks of the central Wyoming Province. Canadian Journal of Earth Sciences 43, 1419–1444.

Fu, J.H., Liu, S.W., Chen, X., Bai, X., Guo, R.R., Wang, W., 2016. Petrogenesis of taxitic dioritic–tonalitic gneisses and Neoarchean crustal growth in Eastern Hebei, North China

Craton. Precambrian Research 284, 64–87.

Fu, J.H., Liu, S.W., Wang, M.J., Chen, X., Guo, B.R., Hu, F.Y., 2017. Late Neoarchean monzogranitic–syenogranitic gneisses in the Eastern Hebei–Western Liaoning Province, North China Craton: Petrogenesis and implications for tectonic setting. Precambrian Research 303, 392-413.

Griffin, W.L., Pearson, N.J., Belousova, E., Jackson, S.E., van Achterbergh, E., O'Reilly, S.Y., Shee, S.R., 2000. The Hf isotope composition of cratonic mantle: LAMMCICPMS analysis of zircon megacrysts in kimberlites. Geochimica et Cosmochimica Acta 64, 133–147.

Guo, B.R., Liu, S.W., Zhang, J., Wang, W., Fu, J.H., Wang, M.J., 2016. Neoarchean Andean-type active continental margin in the northeastern North China Craton: geochemical and geochronological evidence from metavolcanic rocks in the Jiapigou granite–greenstone belt, Southern Jilin Province. Precambrian Research 285, 147–169.

Guo, R.R., Liu, S.W., Wyman, D., Bai, X., Wang, W., Yan, M., Li, Q.G., 2015. Neoarchean subduction: a case study of arc volcanic rocks in QinglongZhuzhangzi area of the Eastern Hebei Province, North China Craton. Precambrian Research 264, 36–62.

Guo, R.R., Liu, S.W., Bai, X., Wang, W., 2017. A Neoarchean subduction recorded by the Eastern Hebei Precambrian basement, North China Craton: Geochemical fingerprints from metavolcanic rocks of the Saheqiao-Shangying-Qinglong supracrustal belt. Precambrian Research 135, 347-369.

Han, C.M., Xiao, W.J., Su, B.X., Sakyi, P.A., Chen, Z.L., Zhang, X.H., Ao, S.J., Zhang, J.E., Wan, B., Zhang, Z.Y., Wang, Z.M., Ding, J.X., 2014. Formation age and genesis of the Gongchangling Neoarchean banded iron deposit in eastern Liaoning Province: constraints

from geochemistry and SHRIMP zircon U-Pb dating. Precambrian Research 254, 306–322

Heilimo, E., Halla, J., Hölttä, P., 2010. Discrimination and origin of the sanukitoid series: geochemical constraints from the Neoarchean western Karelian Province (Finland). Lithos 115, 27–39.

Heilimo, E., Jaana, H., Andersen, T., Huhma, H., 2013. Neoarchean crustal recycling and mantle metasomatism: Hf–Nd–Pb–O isotope evidence from sanukitoids of the Fennoscandian shield. Precambrian Research 228, 250–266.

Hinchey, A.M., Davis, W.J., Ryan, J.J., Nadeau, L., 2011. Neoarchean high-potassium granites of the Boothia mainland area, Rae domain, Churchill Province: U-Pb zircon and Sm–Nd whole rock isotopic constraints. Canadian Journal of Earth Sciences 48, 247–279.

Jiang, N., Guo, J.H., Fan, W.B., Hu, J., Zong, K.Q., Zhang, S.H., 2016. Archean TTGs and sanukitoids from the Jiaobei terrain, North China craton: Insights into crustal growth and mantle metasomatism. Precambrian Research 281, 656-672.

Kumar, K.V., Ernst, W.G., Leelanandam, C., Wooden, J.L., Grove, M.J., 2011. Origin of ~2.5 Ga potassic granite from the Nellore Schist Belt, SE India: textural, cathodoluminescence, and SHRIMP U-Pb data. Contributions to Mineralogy and Petrology 162, 867–888.

LaFlèche, M.R., Camire, G., Jenner, G.A., 1998. Geochemistry of post-Acadian, Carboniferous continental intraplate basalts from the Maritimes basin, Magdalen islands, Quebec, Canada. Chemical Geology 148, 115–136.

Laurent, O., Martin, H., Doucelance, R., Moyen, J.F., Paquette, J.L., 2011. Geochemistry and petrogenesis of high-K “sanukitoids” from the Bulai pluton, Central Limpopo Belt, South Africa: implications for geodynamic change at the Archaean–Proterozoic boundary. Lithos 123,

73–91.

Laurent, O., Martin, H., Moyen, J.F., Doucelance, R., 2014. The diversity and evolution of late-Archean granitoids: evidence for the onset of ‘‘modern-style” plate tectonics between 3.0 and 2.5 Ga. Lithos 205, 208–235.

Liu, D.Y., Nutman, A.P., Compston, W., Wu, J.S., Shen, Q.H., 1992. Remnants of ～3800 Ma crust in the Chinese part of the Sino-Korean craton. Geology 20, 339–342.

Lin, Q., Wu, F.Y., Liu, S.W., Ge, W.C., Sun, J.G., Yin, J.Z., 1992. Archean Granites in the East of North China Platform. Science Press, Beijing (in Chinese).

Liou, P., Guo, J.H., Huang, G.Y., Fan, W.B., 2017. 2.9 Ga magmatism in Eastern Hebei, North China Craton. Precambrian Research https://doi.org/10.1016/j.precamres.2017.11.002.

Liu, S.W., Pan, Y.M., Xie, Q.L., Zhang, J., Li, Q.G., 2004. Archean geodynamics in the Central Zone, North China craton: constraints from geochemistry of two contrasting series of granitoids in the Fuping and Wutaishan complexes. Precambrian Research 130, 229–249.

Liu, S.W., Wang, W., Bai, X., Zhang, F., 2010. Geological events of early Precambrian complex in North Chaoyang area, Liaoning Province. Acta Petrologica Sinica 26, 1993–2004 (in Chinese with English abstract).

Liu, S.W., Santosh, M., Wang, W., Bai, X., Yang, P.T., 2011. Zircon U-Pb chronology of the Jianping Complex: implications for the Precambrian crustal evolution history of the northern margin of North China Craton. Gondwana Research 20, 48–63.

Liu, S.W., Fu, J.H., Sun, G.Z., Gao, L., Hu, Y.L., 2018. Petrogenesis and geodynamics of Archean sanukitoid gneisses in the Jinzhou-Qian’an area. Acta Petrologica Sinica 34, 1083-1098.

Lobach-Zhuchenko, S.B., Rollinson, H., Chekulaev, V.P., Savatenkov, V.M., Kovalenko, A.V.,

Martin, H., Guseva, N.S., Arestova, N.A., 2008. Petrology of Late Archean, highly potassic, sanukitoid pluton from the Baltic Shield: insights into Late Archean mantle metasomatism. Journal of Petrology 49, 393–420.

Maniar, P.D., Piccoli, P.M., 1989. Tectonic discrimination of granitoids. Geological Society of America Bulletin 101, 635–643.

Martin, H., Smithies, R.H., Moyen, J.F., Champion, D., 2005. An overview of adakite, tonalite–trondhjemite–granodiorite (TTG), and sanukitoid: relationships and some implications for crust evolution. Lithos 79, 1–24.

Martin, H., Moyen, J.F., Rapp, R., 2009. The sanukitoid series: magmatism at the Archaean-Proterozoic transition. Earth and Environmental Science Transactions of the Royal Society of Edinburgh 100, 15–33.

Martin, H., Moyen, J.F., Guitreau, M., Blichert-Toft, J., Le Pennec, J.L., 2014. Why Archaean TTG cannot be generated by MORB melting in subduction zones. Lithos 198–199, 1–13.

Middlemost, E.A.K., 1994. Naming materials in the magma/igneous rock system. Earth-Science Reviews 37, 215–224.

Mikkola, P., Heilimo, E., Huhma, H., 2014. Relationships between sanukitoids and crust-derived melts and their implications for the diversity of Neoarchaean granitoids: a case study from Surmansuo and nearby areas, Eastern Finland. Bulletin of the Geological Society of Finland 86, 23–40.

Moyen, J.F., 2011. The composite Archaean grey gneisses: petrological significance, and evidence for a non-unique tectonic setting for Archaean crustal growth. Lithos 123, 21–36.

Moyen, J.F., Martin, H., 2012. Forty years of TTG research. Lithos 148, 312–336.

Nutman, A.P., Wan, Y.S., Du, L.L., Friend, C.R.L., Dong, C.Y., Xie, H.Q., Wang, W., Sun, H.Y., Liu, D.Y., 2011. Multistage late Neoarchaean crustal evolution of the North China Craton, eastern Hebei. Precambrian Research 189, 43–65.

Qian, Q., Hermann, J., 2013. Partial melting of lower crust at 10–15 kbar: constraints on adakite and TTG formation. Contributions to Mineralogy and Petrology 165, 1195–1224.

Rapp, R.P., Watson, E.B., 1995. Dehydration melting of metabasalt at 8–32 kbar: implications for continental growth and crust–mantle recycling. Journal of Petrology 36, 891–931.

Rapp, R.P., Shimizu, N., Norman, M.D., 2003. Growth of early continental crust by partial melting of eclogite. Nature 425, 605–609.

Rapp, R.P., Norman, M.D., Laporte, D., Yaxley, G.M., Martin, H., Foley, S.F., 2010. Continent formation in the Archean and chemical evolution of the Cratonic lithosphere: melt-Rock reaction experiments at 3–4 GPa and petrogenesis of Archean Mg-Diorites (Sanukitoids). Journal of Petrology 51, 1237–1266.

Rollinson, H.R., 1993. Using Geochemical Data: Evaluation, Presentation, Interpretation. Routledge.

Romano, R., Lana, C., Alkmim, F.F., Stevens, G., Armstrong, R., 2013. Stabilization of the southern portion of the São Francisco craton, SE Brazil, through a long-lived period of potassic magmatism. Precambrian Research 224, 143-159.

Schiano, P., Monzier, M., Eissen, J.P., Martin, H., Koga, K.T., 2010. Simple mixing as the major control of the evolution of volcanic suites in the Ecuadorian Andes. Contributions to Mineralogy and Petrology 160, 297–312.

Semprich, J., Moreno, J.A., Oliveira, E.P., 2015. Phase equilibria and trace element modeling of

Archean sanukitoid melts. Precambrian Research 269, 122–138.

Shirey, S.B., Hanson, G.N., 1984. Mantle-derived Archaean monzodiorites and trachyandesites. Nature 310, 222–224.

Sisson, T.W., Ratajeski, K., Hankins, W.B., Glazner, A.F., 2005. Voluminous granitic magmas from common basaltic sources. Contributions to Mineralogy and Petrology 148, 635–661.

Smithies, R.H., 2000. The Archean tonalite–trondhjemite–granodiorite (TTG) series is not an analogue of Cenozoic adakite. Earth and Planetary Science Letters 182, 115–125.

Smithies, R.H., Champion, D.C., 2000. The Archaean high-Mg diorite suite: links to tonalite–trondhjemite–granodiorite magmatism and implications for early Archaean crustal growth. Journal of Petrology 41, 1653–1671.

Smithies, R.H., Kranendonk, M.J., Champion, D.C., 2007. The Mesoarchean emergence of modern-style subduction. Gondwana Research 11, 50–68.

Stern, R.A., Hanson, G.N., 1991. Archean high-Mg granodiorite: a derivative of light rare earth element-enriched Monzodiorite of mantle origin. Journal of Petrology 32, 201–238.

Sun, S.S., McDonough, W.F., 1989. Chemical and isotopic systematics of oceanic basalts: implications for mantle composition and processes. Geological Society of London Special Publications 42, 313–345.

Wang, C., Song, S.G., Niu, Y.L., Wei, C.J., Su, L., 2016. TTG and Potassic Granitoids in the Eastern North China Craton: Making Neoarchean Upper Continental Crust during Micro-continental Collision and Post-collisional Extension. Journal of Petrology 57, 1775-1810.

Wang, M.J., Liu, S.W., Fu, J.H., Wang, K., Guo, R.R., Guo, B.R., 2017. Neoarchean DTTG

gneisses in southern Liaoning Province and their constraints on crustal growth and the nature of the Liao-Ji Belt in the Eastern Block. Precambrian Research 303, 183-207.

Wang, W., Liu, S.W., Bai, X., Yang, P.T., Li, Q.G., Zhang, L.F., 2011. Geochemistry and zircon U-Pb–Hf isotopic systematics of the Neoarchean Yixian-Fuxin greenstone belt, northern margin of the North China Craton: implications for petrogenesis and tectonic setting. Gondwana Research 20, 64–81.

Wang, W., Liu, S.W., Wilde, S.A., Li, Q.G., Zhang, J., Bai, X., Yang, P.T., Guo, R.R., 2012. Petrogenesis and geochronology of Precambrian granitoid gneisses in Western Liaoning Province: constraints on Neoarchean to early Paleoproterozoic crustal evolution of North China Craton. Precambrian Research 222–223, 290–311.

Wang, W., Liu, S.W., Santosh, M., Bai, X., Li, Q.G., Yang, P.T., Guo, R.R., 2013. Zircon U–Pb–Hf isotopes and whole-rock geochemistry of granitoid gneisses in the Jianping gneissic terrane, Western Liaoning Province: constraints on the Neoarchean crustal evolution of the North China Craton. Precambrian Research 224, 184–221.

Wang, W., Liu, S.W., Santosh, M., Wang, G.H., Bai, X., Guo, R.R., 2015. Neoarchean intra-oceanic arc system in the Western Liaoning Province: implications for the Early Precambrian crust–mantle geodynamic evolution of the Eastern Block of the North China Craton. Earth-Science Reviews 150, 329–364.

Wang, Y.J., Zhang, Y.Z., Zhao, G.C., Fan, W.M., Xia, X.P., Zhang, F.F., Zhang, A.M., 2009. Zircon U–Pb geochronological and geochemical constraints on the petrogenesis of the Taishan sanukitoids (Shandong): implications for Neoarchean subduction in the Eastern Block, North China Craton. Precambrian Research 174, 273–286.

Wu, M.L., Zhao, G.C., Sun, M., Li, S.Z., He, Y.H., Bao, Z.A., 2013. Zircon U-Pb geochronology and Hf isotopes of major lithologies from the Yishui Terrane: implications for the crustal evolution of the Eastern Block, North China Craton. Lithos 170–171, 164–178.

Xiong, X.L., Keppler, H., Audétat, A., Gudfinnsson, G., Sun, W.D., Song, M.S., Xiao, W.S., Yuan, L., 2009. Experimental constraints on rutile saturation during partial melting of metabasalt at the amphibolite to eclogite transition, with applications to TTG genesis. American Mineralogist 94, 1175–1186.

Yang, J.H., Wu, F.Y., Wilde, S.A., Zhao, G.C., 2008. Petrogenesis and geodynamics of Late Archean magmatism in eastern Hebei, eastern North China Craton: geochronological, geochemical and Nd–Hf isotopic evidence. Precambrian Research 167, 125–149.

Zhai, M.G., Santosh, M., 2011. The early Precambrian odyssey of the North China Craton: a synoptic overview. Gondwana Research 20, 6–25.

Zhai, M.G., Santosh, M., 2013. Metallogeny of the North China Craton: link with secular changes in the evolving Earth. Gondwana Research 24, 275–297.

Zhang, Y.Y., Cai, L.B., Jin, W., Liu, T., Zheng, P.X., Li, J., 2016. The petrogenesis and evolutionary process of Neoarchean Diaoyutai granite in western Liaoning Province: evidences from petrofabric. Acta Petrologica Sinica 32, 2867–2880 (in Chinese with English abstract).

Zhao, G.C., Sun, M., Wilde, S.A., Li, S.Z., 2005. Late Archean to Paleoproterozoic evolution of the North China Craton: key issues revisited. Precambrian Research 136, 177–202.

Zhao, G.C., Cawood, P.A., Li, S.Z., Wilde, S.A., Sun, M., Zhang, J., He, Y.H., Yin, C.Q., 2012. Amalgamation of the North China Craton: key issues and discussion. Precambrian Research 222–223, 55–76.

Figure captions

Fig. 1. (A) Tectonic subdivision of North China Craton (modified from Zhao et al. (2005, 2012) and Wu et al. (2013)). Archean crystalline basement of the Western Liaoning Province (Fig. 1B) is shown by the rectangle. (B) Simplified geological map and Neoarchean lithological zonation of the Western Liaoning basement terranes. (C) Simplified geological map of the Neoarchean basement in the southeastern zone, showing the distribution of porphyritic monzodioritic-quartz monzodioritic-granodioritic-monzogranitic (MQGM) gneisses and the locations of the samples for which zircon U–Pb and Lu–Hf isotopic analyses were conducted. Abbreviations: CD-Chengde; DF-Dengfeng; EH-Eastern Hebei; FP-Fuping; HA-Huai'an; HS-Hengshan; JD-Jiaodong; LL-Lvliang; NH-Northern Hebei; NL-Northern Liaoning; SJ-Southern Jilin; SL-Southern Liaoning; TH-Taihua; WL-Western Liaoning; WT-Wutai; WS-Western Shandong; XH-Xuanhua; ZH-Zanhuang; ZT-Zhongtiao.

Fig. 2. Field photographs showing geological relationships and macroscopic lithological features of the porphyritic MQGM gneisses and TTG xenoliths in the southeastern zone. (A) BDG porphyritic monzogranitic rock intruding the tonalitic gneiss, as indicated by the monzogranitic apophysis cutting the foliations of the tonalitic gneiss and the tonalitic xenolith within the monzogranitic apophysis. (B) Supracrustal amphibolite xenolith within the ADG porphyritic granodioritic gneiss. (C) ADG porphyritic monzodioritic gneiss. (D) ADG porphyritic monzogranitic gneiss. (E) BDG porphyritic granodioritic gneiss. (F) Intrusive contract between BDG porphyritic monzogranitic gneiss and medium-grained monzogranites.

The diameter of lens cover and the length of hammer are about 5 cm and 40 cm, respectively.

Fig. 3. Photomicrographs showing petrographic features of representative porphyritic MQGM gneisses and TTG xenolith. (A) tonalitic gneiss sample 15LX21-1. (B) ADG porphyritic monzodioritic gneiss sample 15LX19-1. (C) ADG porphyritic quartz monzodioritic gneiss sample 15LX19-2. (D) BDG porphyritic granodioritic gneiss sample 15LX52-1. (E) BDG porphyritic monzogranitic gneiss sample 15LX38-1. (F) Euhedral magmatic epidote partially enclosed by biotite. Mineral abbreviations are as follows: Pth, perthite; Mc, microcline; Pl, plagioclase; Qtz, quartz; Amp, amphibole; Bi, biotite; Ep, epidote.

Fig. 4. Major element compositions of the porphyritic MQGM gneisses and tonalitic gneiss xenolith in the southeastern zone. (A) An–Ab–Or diagram (Barker, 1979). (B) Total alkali versus silica diagram (TAS, after Middlemost, 1994). (C) K_2O versus SiO_2 classification diagram (after Rollinson, 1993). Archean sanukitoids after Martin et al. (2009). (D) MgO versus SiO_2 diagram (PMB, experimental partial melts of basalts from Bread and Lofgren (1989, 1991), Rapp and Watson (1995), and Qian and Hermann (2013); HSA, high-silica adakite after Martin et al. (2005); Sanukitoids after Martin et al. (2009)). (E) Mg# (100 $Mg/(Mg+Fe_{total})$ in atomic ratio) versus SiO_2 diagram. (F) A/NK (molar $Al_2O_3/(Na_2O+K_2O)$) versus A/CNK ($Al_2O_3/(CaO+Na_2O+K_2O)$) diagram (after Maniar and Piccoli, 1989).

Fig. 5. Chondrite-normalized REE patterns and primitive mantle-normalized spider diagrams for (A and B) the tonalitic gneiss xenolith and ADG samples, and (C and D) the BDG samples.

Symbols are the same as Fig. 4, and chondrite and primitive mantle values after Sun and McDonough (1989).

Fig. 6. Cathodoluminescence images of representative zircon grains from tonalitic gneiss 15LX21-1 (A), ADG granodioritic gneiss 15LX01-2 (B), ADG quartz monzodioritic gneiss 15LX19-2 (C), ADG granodioritic gneiss 15LX88-1 (D), BDG granodioritic gneiss 15LX03-1 (E), BDG monzogranitic gneiss 15LX38-1 (F), BDG granodioritic gneisses 15LX47-1 (G) and 15LX52-1 (H), and BDG monzogranitic gneiss 15LX54-1 (I), showing the inner structures, analyzed locations and corresponding apparent $^{207}Pb/^{206}Pb$ ages.

Fig. 7. Concordia diagrams showing LA-ICP-MS zircon U–Pb isotopic dating data and calculated ages for representative porphyritic MQGM gneisses and tonalitic gneiss xenolith in the southeastern zone: (A) 15LX21-1, (B) 15LX01-2, (C) 15LX19-2, (D) 15LX88-1, (E) 15LX03-1, (F) 15LX38-1, (G) 15LX47-1, (H) 15LX52-1, and (I) 15LX54-1.

Fig. 8. Plots of zircon $\varepsilon Hf(t)$ values versus crystallization ages for the nine dated porphyritic MQGM gneisses and tonalitic gneiss xenolith: (A) 15LX21-1, (B) 15LX01-2, (C) 15LX19-2, (D) 15LX88-1, (E) 15LX03-1, (F) 15LX38-1, (G) 15LX47-1, (H) 15LX52-1, and (I) 15LX54-1. Note that Lu–Hf isotopic data of the inherited zircon spots are corrected to their respective apparent $^{207}Pb/^{206}Pb$ ages, whereas those of the other analyzed spots are corrected to their magmatic crystallization ages. $^{176}Lu/^{177}Hf$ ratios of the depleted mantle and chondrite are 0.0384 and 0.0332, respectively, after Blichert-Toft and Albarède (1997) and Griffin et al.

(2000).

Fig. 9. Petrogenetic discrimination diagrams for the porphyritic MQGM gneisses and tonalitic gneiss xenolith. (A) MALI index (Na_2O+K_2O-CaO) versus SiO_2 diagram (Laurent et al., 2014), showing geochemical affinities between the ADG samples and sanukitoids. (B) Na_2O/K_2O-2*A/CNK-2*FMSB ($(FeO_t+MgO)_{wt.\%}$*$(Sr+Ba)_{wt.\%}$) ternary diagrams (Laurent et al., 2014), showing the geochemical differences among the tonalitic gneiss, ADG samples, and BDG samples. (C) Sum of "mafic" oxides ($FeO_t+MgO+MnO+TiO_2$) versus SiO_2 diagram (Laurent et al., 2014), showing geochemical affinities between the ADG samples and sanukitoids. (D) La/Sm versus La (ppm) and (E) Cs/Sm versus Cs (ppm) diagrams, showing that the geochemical variations of the ADG samples and BDG samples are mainly controlled by partial melting processes (Schiano et al., 2010). The inset is a schematic C^H/C^M versus C^H plot, with C^H and C^M as concentrations of highly and moderately incompatible elements, respectively. (F) $(Hf/Sm)_N$ versus $(Nb/La)_N$ diagram (LaFlèche et al., 1998). The geochemical parameters for N-MORB, E-MORB and OIB are after Sun and McDonough (1989). (G) Molar $Al_2O_3/(MgO+FeO_t)$ (AFM) versus molar $CaO/(MgO+FeO_t)$ (CFM) diagram, showing the source compositions of the BDG samples (modified after Altherr et al., (2000)). (H) 3*CaO-$Al_2O_3/(FeO_t+MgO)$-5*K_2O/Na_2O ternary diagrams (Laurent et al., 2014), showing the source compositions of the BDG samples. Symbols are the same as Fig. 4.

Fig. 10. Age distributions and temporal relationships among various lithological assemblages in the Neoarchean basement of the Western Liaoning Province, northern NCC. Data from Liu

et al. (2011), Wang et al. (2011, 2012, 2013, 2015) and this paper.

Fig. 11. A Neoarchean active continental margin tectonic model for the southeastern zone of the Western Liaoning Province, northern NCC. The partial melts from subducted oceanic slabs interacted with the mantle wedge, resulting in the generation of the ～2563 Ma TTG gneisses. The partial melting of lithospheric mantle metasomatized by dehydration fluids and melts derived from subducted oceanic sediments and slabs and the partial melting of medium-K to high-K mafic rocks gave birth to the 2546-2529 Ma porphyritic MQGM gneisses. The partial melting of porphyritic MQGM gneisses resulted in the formation of the 2527-2511 Ma monzogranite-syenogranites. See text for details.

Table 1. Petrological features of the TTG xenolith and porphyritic MQGM gneisses

Sample	Category		Lithology	Latitude (N)	Longitude(E)	Mineral assemblage
15LX21-1	TTG xenoliths		Tonalitic gneiss	40°53′04″	121°03′25″	Qtz(24%)+Kfs(6%)+Pl(54%)+Amp(3%)+Bi(13%)
15LX01-1	Porphyritic MQGM gneisses	ADG samples	Quartz monzodioritic gneiss	41°11′36″	121°18′57″	Qtz(15%)+Kfs(20%)+Pl(48%)+Amp(12%)+Bi(5%)
15LX01-2			Granodioritic gneiss	41°11′36″	121°18′57″	Qtz(23%)+Kfs(18%)+Pl(44%)+Amp(10%)+Bi(5%)
15LX08-1			Granodioritic gneiss	41°18′01″	121°24′14″	Qtz(21%)+Kfs(19%)+Pl(40%)+Amp(13%)+Bi(7%)
15LX08-2			Granodioritic gneiss	41°18′01″	121°24′14″	Qtz(23%)+Kfs(19%)+Pl(43%)+Amp(9%)+Bi(6%)
15LX10-1			Monzogranitic gneiss	41°09′59″	121°15′34″	Qtz(22%)+Kfs(23%)+Pl(39%)+Amp(11%)+Bi(5%)
15LX13-2			Monzogranitic gneiss	41°07′16″	121°15′25″	Qtz(23%)+Kfs(27%)+Pl(36%)+Amp(9%)+Bi(5%)
15LX18-1			Monzogranitic gneiss	41°00′11″	121°05′09″	Qtz(23%)+Kfs(26%)+Pl(39%)+Amp(9%)+Bi(5%)
15LX19-1			Monzodioritic gneiss	40°55′39″	121°05′20″	Qtz(4%)+Kfs(17%)+Pl(56%)+Amp(16%)+Bi(7%)
15LX19-2			Quartz monzodioritic gneiss	40°55′39″	121°05′20″	Qtz(14%)+Kfs(16%)+Pl(53%)+Amp(13%)+Bi(4%)
15LX21-2			Monzogranitic gneiss	40°53′04″	121°03′25″	Qtz(22%)+Kfs(25%)+Pl(41%)+Amp(8%)+Bi(6%)
15LX44-1			Monzogranitic gneiss	40°49′20″	120°45′14″	Qtz(20%)+Kfs(24%)+Pl(41%)+Amp(11%)+Bi(4%)
15LX88-1			Granodioritic gneiss	40°30′47″	120°49′16″	Qtz(22%)+Kfs(15%)+Pl(45%)+Amp(10%)+Bi(8%)
15LX03-1		BDG samples	Granodioritic gneiss	41°10′02″	121°19′02″	Qtz(21%)+Kfs(21%)+Pl(43%)+Amp(6%)+Bi(9%)
15LX17-3			Monzogranitic gneiss	41°02′21″	121°04′20″	Qtz(26%)+Kfs(23%)+Pl(41%)+Amp(3%)+Bi(7%)
15LX21-3			Monzogranitic gneiss	40°53′04″	121°03′25″	Qtz(26%)+Kfs(29%)+Pl(37%)+Amp(3%)+Bi(5%)
15LX27-1			Monzogranitic gneiss	41°04′32″	121°12′04″	Qtz(25%)+Kfs(23%)+Pl(42%)+Amp(3%)+Bi(7%)
15LX31-1			Monzogranitic gneiss	40°47′33″	120°39′44″	Qtz(24%)+Kfs(26%)+Pl(35%)+Amp(2%)+Bi(13%)
15LX31-2			Granodioritic gneiss	40°47′33″	120°39′44″	Qtz(24%)+Kfs(20%)+Pl(44%)+Bi(12%)
15LX			Monzogranitic	40°54′	120°49	Qtz(24%)+Kfs(23%)+Pl(38%)+A

36-2		gneiss	29″	′ 53″	mp(5%)+Bi(10%)
15LX		Monzogranitic	40°52′	120°48	Qtz(23%)+Kfs(25%)+Pl(39%)+A
38-1		gneiss	30″	′ 29″	mp(5%)+Bi(8%)
15LX		Granodioritic	40°36′	120°47	Qtz(22%)+Kfs(20%)+Pl(47%)+B
47-1		gneiss	04″	′ 35″	i(11%)
15LX		Granodioritic	40°32′	120°29	Qtz(25%)+Kfs(21%)+Pl(44%)+A
52-1		gneiss	54″	′ 05″	mp(3%)+Bi(7%)
15LX		Monzogranitic	40°28′	120°21	Qtz(26%)+Kfs(27%)+Pl(37%)+B
54-1		gneiss	15″	′ 03″	i(10%)
15LX		Granodioritic	40°22′	120°35	Qtz(24%)+Kfs(19%)+Pl(43%)+A
86-1		gneiss	08″	′ 19″	mp(6%)+Bi(8%)
15LX		Monzogranitic	40°29′	120°46	Qtz(23%)+Kfs(24%)+Pl(43%)+B
89-2		gneiss	41″	′ 52″	i(10%)

Notes: Qtz, quartz; Kfs, K-feldspar; Pl, plagioclase; Amp, amphibole; Bi, biotite.

Research Highlights:

- Neoarchean basement in the Western Liaoning Province displays prominent zonation.
- 2563 Ma tonalitic gneiss xenolith formed by slab melt contaminated by mantle peridotite.
- 2546-2529 Ma sanukitoids stemmed from metasomatized lithospheric mantle.
- 2546-2531 Ma potassic granites formed by melting of medium- to high-K mafic rocks.
- Neoarchean active continental margin setting in southeastern Western Liaoning Province.

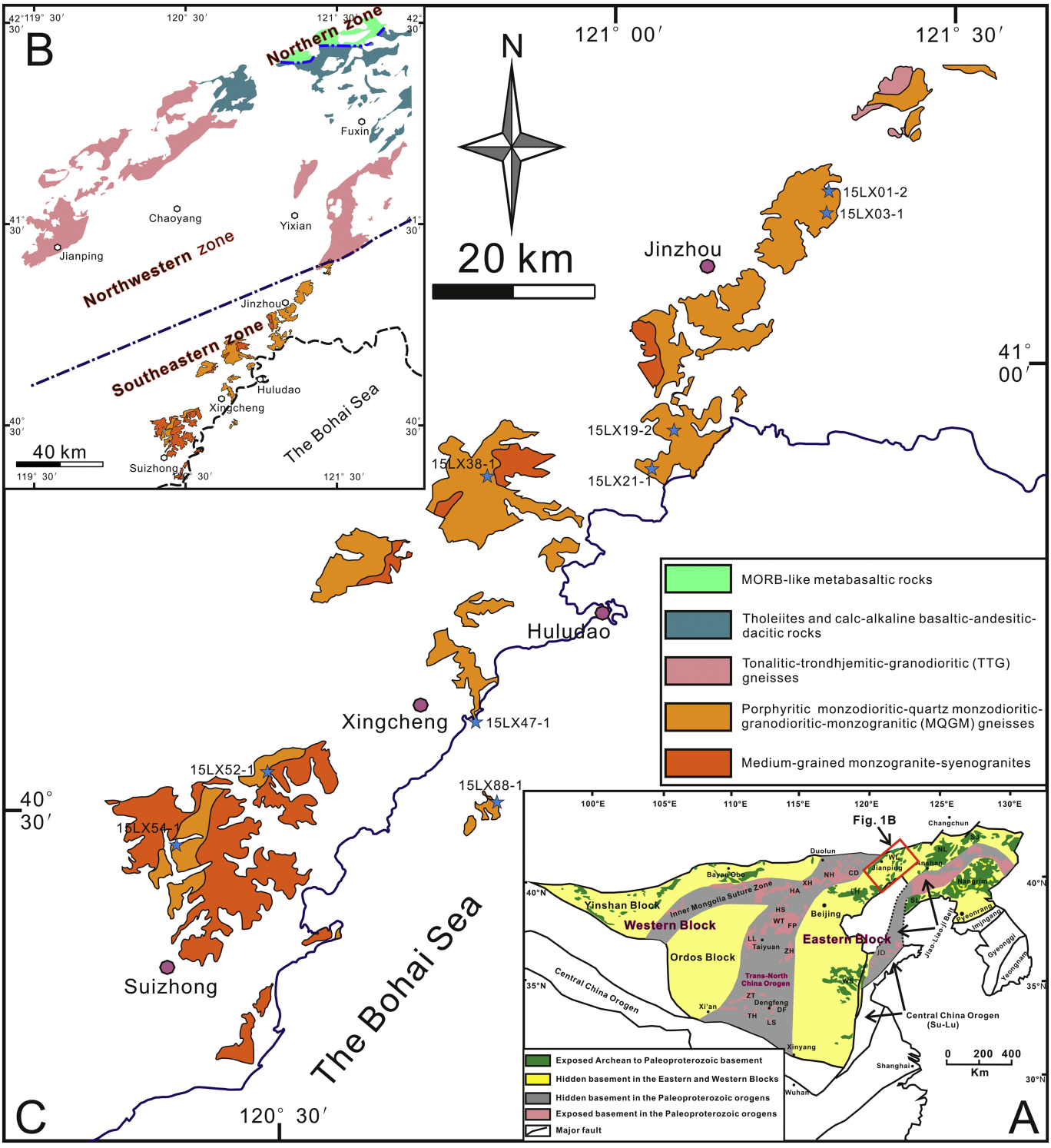
B
Northern zone
Fuxin
Chaoyang
Yixian
Jianping
Northwestern zone
Jinzhou
Southeastern zone
Huludao
Xingcheng
Suizhong
The Bohai Sea
40 km
119° 30′
120° 30′
121° 30′
42° 30′
41° 30′
40° 30′
N
20 km
121° 00′
121° 30′
41° 00′
40° 30′
15LX01-2
15LX03-1
Jinzhou
15LX19-2
15LX21-1
15LX38-1
Huludao
Xingcheng
15LX47-1
15LX52-1
15LX54-1
15LX88-1
Suizhong
The Bohai Sea
120° 30′
C
MORB-like metabasaltic rocks
Tholeiites and calc-alkaline basaltic-andesitic-dacitic rocks
Tonalitic-trondhjemitic-granodioritic (TTG) gneisses
Porphyritic monzodioritic-quartz monzodioritic-granodioritic-monzogranitic (MQGM) gneisses
Medium-grained monzogranite-syenogranites
Fig. 1B
Yinshan Block
Western Block
Ordos Block
Inner Mongolia Suture Zone
Trans-North China Orogen
Central China Orogen
Eastern Block
Beijing
Taiyuan
Xi'an
Dengfeng
Xinyang
Changchun
Duolun
Shanghai
Wuhan
Jiao-Liao-Ji Belt
Liaonorang
Imjingang
Gyeonggi
Yeongnam
Central China Orogen (Su-Lu)
0 200 400 Km
Exposed Archean to Paleoproterozoic basement
Hidden basement in the Eastern and Western Blocks
Hidden basement in the Paleoproterozoic orogens
Exposed basement in the Paleoproterozoic orogens
Major fault
A

Figure 1

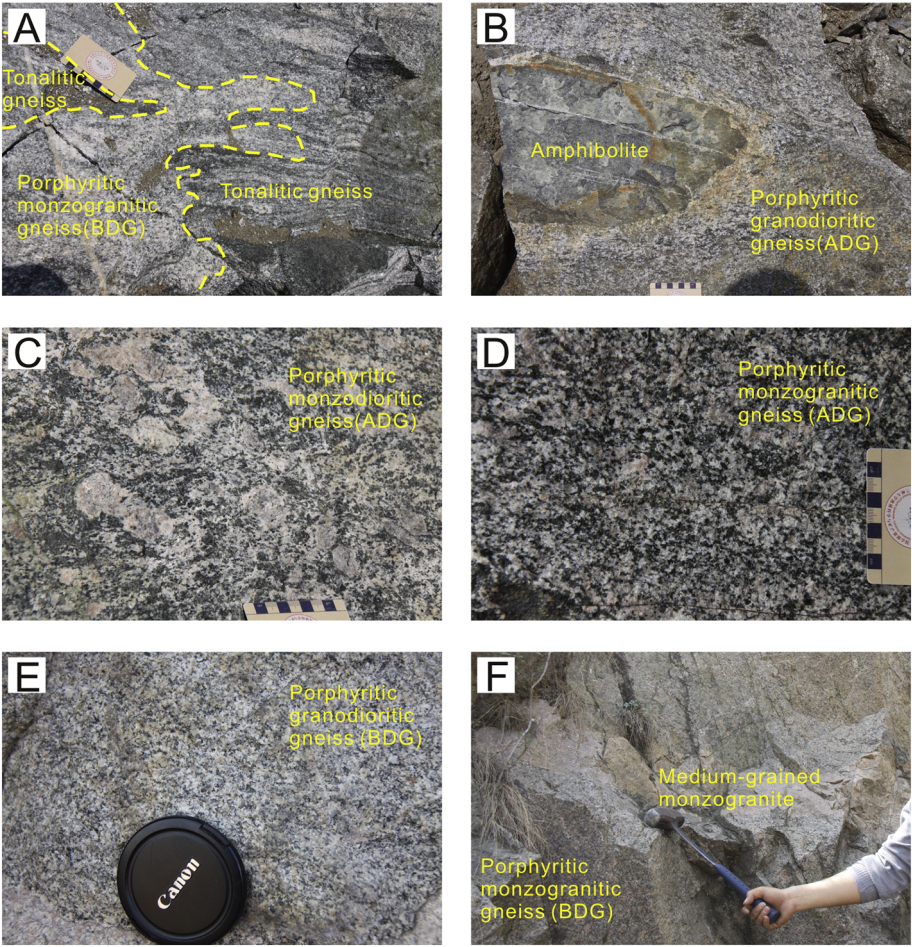
A
Tonalitic gneiss
Porphyritic monzogranitic gneiss(BDG)
Tonalitic gneiss
B
Amphibolite
Porphyritic granodioritic gneiss(ADG)
C
Porphyritic monzodioritic gneiss(ADG)
D
Porphyritic monzogranitic gneiss (ADG)
E
Porphyritic granodiontic gneiss (BDG)
Canon
F
Medium-grained monzogranite
Porphyritic monzogranitic gneiss (BDG)

Figure 2

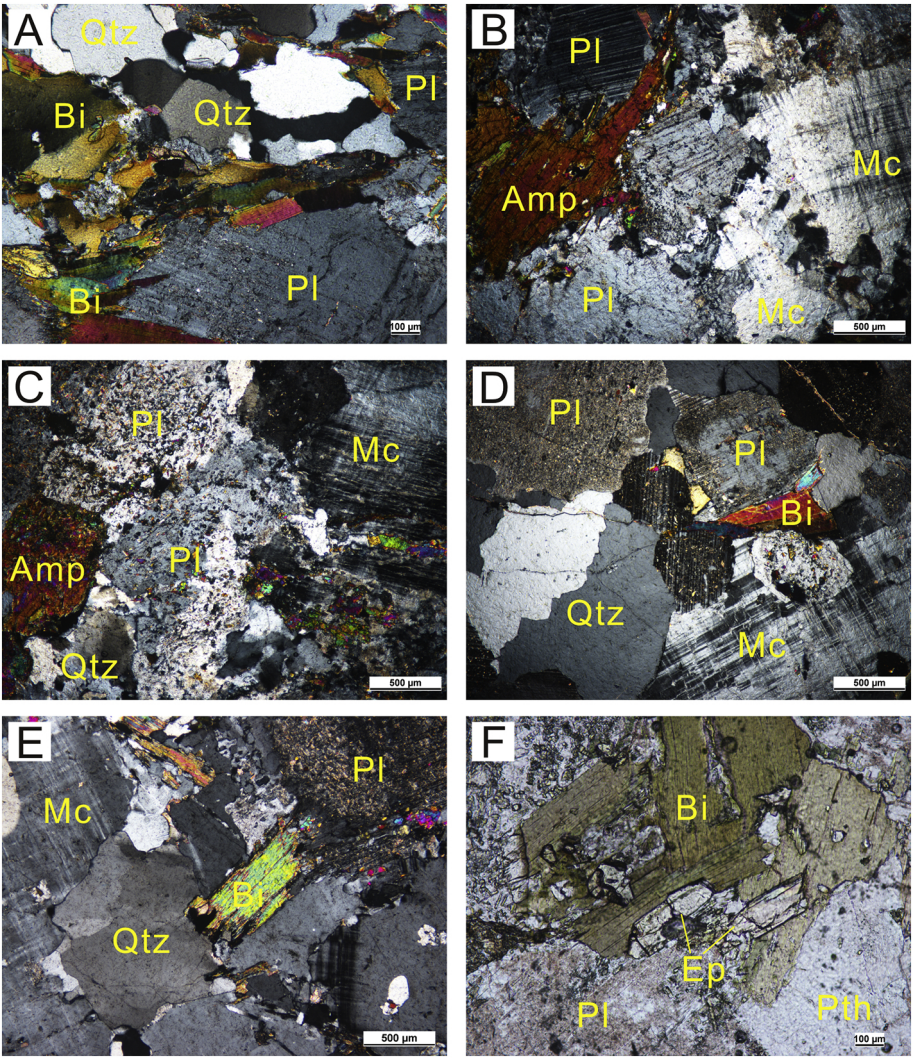
A
Qtz
Pl
Bi
Qtz
Bi
Pl
100 µm
B
Pl
Mc
Amp
Pl
Mc
500 µm
C
Pl
Mc
Amp
Pl
Qtz
500 µm
D
Pl
Pl
Bi
Qtz
Mc
500 µm
E
Pl
Mc
Bi
Qtz
500 µm
F
Bi
Ep
Pl
Pth
100 µm

Figure 3

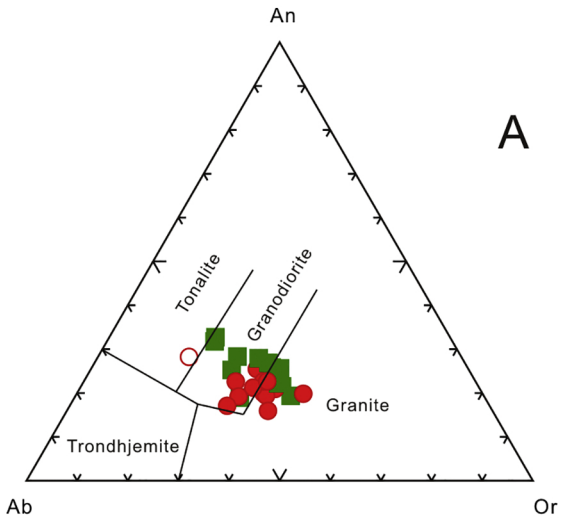
An
A
Tonalite
Granodiorite
Granite
Trondhjemite
Ab
Or

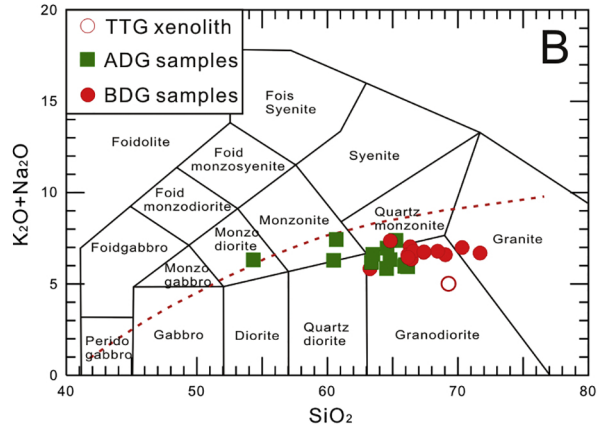
TTG xenolith
ADG samples
BDG samples
B
Fois Syenite
Foidolite
Foid monzosyenite
Syenite
Foid monzodiorite
Monzonite
Quartz monzonite
Granite
Foidgabbro
Monzo diorite
Monzo gabbro
Perido gabbro
Gabbro
Diorite
Quartz diorite
Granodiorite
K2O+Na2O
SiO2

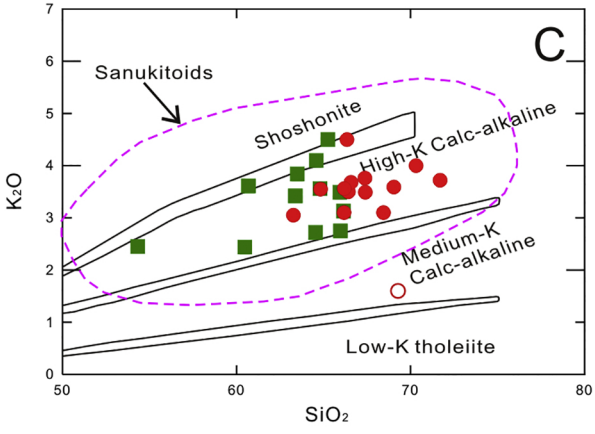
C
Sanukitoids
Shoshonite
High-K Calc-alkaline
Medium-K Calc-alkaline
Low-K tholeiite
K2O
SiO2

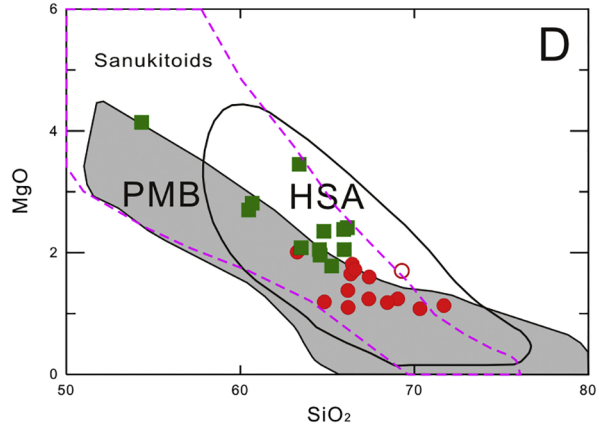
D
Sanukitoids
PMB
HSA
MgO
SiO2

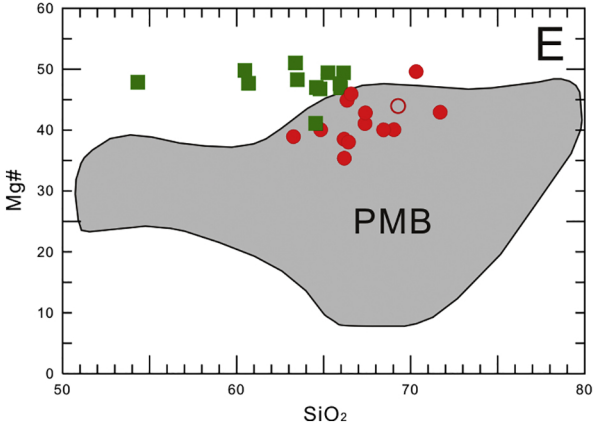
E
PMB
Mg#
SiO2

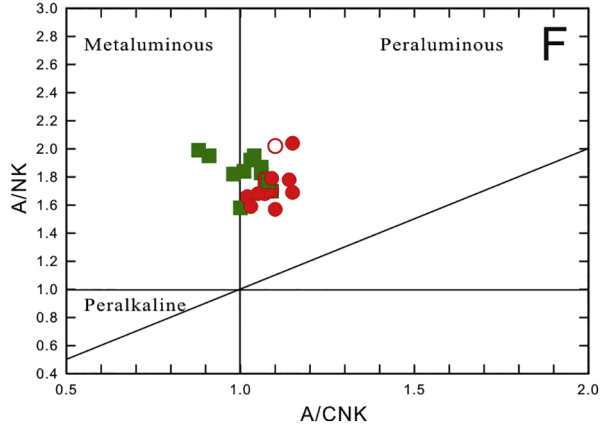
F
Metaluminous
Peraluminous
Peralkaline
A/NK
A/CNK

Figure 4

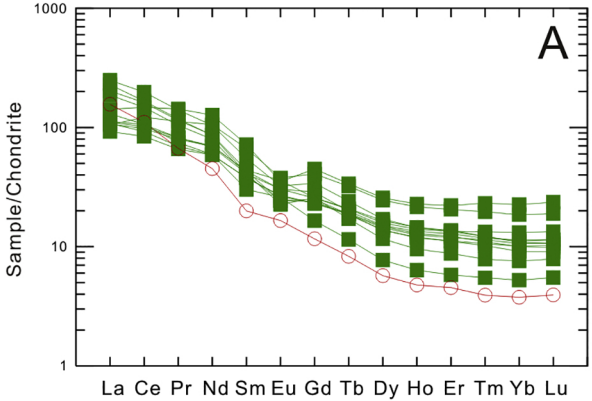
A
Sample/Chondrite
1000
100
10
1
La Ce Pr Nd Sm Eu Gd Tb Dy Ho Er Tm Yb Lu

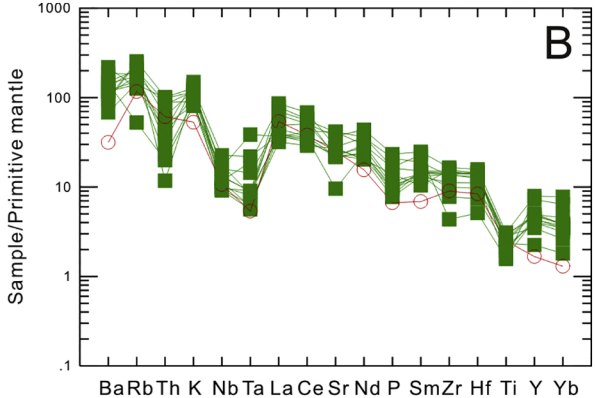
B
Sample/Primitive mantle
1000
100
10
1
.1
Ba Rb Th K Nb Ta La Ce Sr Nd P Sm Zr Hf Ti Y Yb

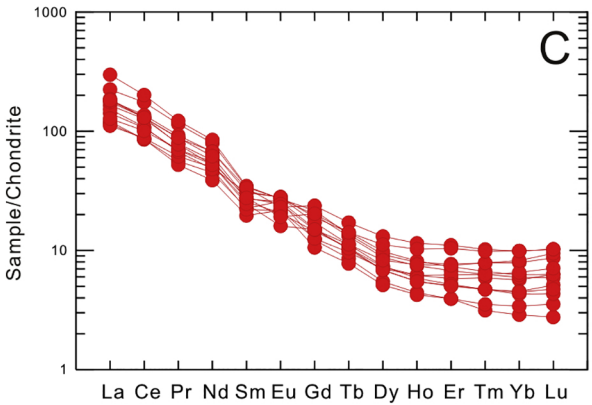
C
Sample/Chondrite
1000
100
10
1
La Ce Pr Nd Sm Eu Gd Tb Dy Ho Er Tm Yb Lu

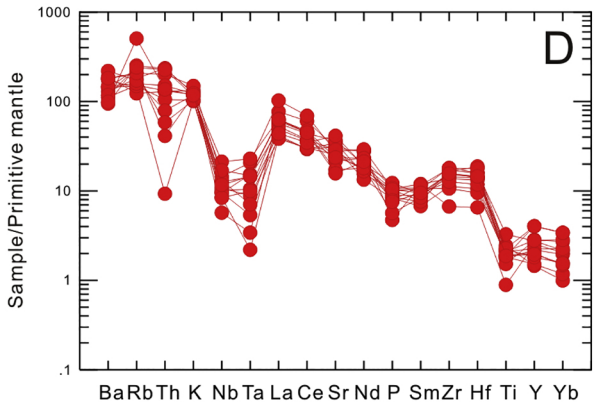
D
Sample/Primitive mantle
1000
100
10
1
.1
Ba Rb Th K Nb Ta La Ce Sr Nd P Sm Zr Hf Ti Y Yb

Figure 5


A Sample 15LX21-1
80 um
2502±16 Ma
#28
#29
#24
#05
2695±15 Ma
2578±15 Ma
2573±15 Ma
#19
#22
#17
2560±15 Ma
2560±16 Ma
2501±16 Ma
B Sample 15LX01-2
100 um
2500±16 Ma
#25
#26
#22
#08
2548±16 Ma
2545±16 Ma
2541±16 Ma
#07
#03
#19
2537±16 Ma
2524±16 Ma
2517±16 Ma
C Sample 15LX19-2
100 um
#05
#23
2543±14 Ma
2533±14 Ma
2531±15 Ma
#21
#18
#24
2521±14 Ma
2510±14 Ma
2497±14 Ma
D Sample 15LX88-1
100 um
#27
#14
#15
2549±16 Ma
2546±15 Ma
2545±15 Ma
#10
#30
#02
2544±15 Ma
2544±15 Ma
2543±15 Ma
E Sample 15LX03-1
100 um
#16
#02
#23
2538±15 Ma
2536±15 Ma
2534±15 Ma
#12
#27
#03
2529±15 Ma
2524±16 Ma
2512±15 Ma
F Sample 15LX38-1
100 um
2541±16 Ma
#24
#25
#17
#14
2555±15 Ma
2554±16 Ma
2550±16 Ma
2485±51 Ma
#18
#27
#26
#09
2539±17 Ma
2538±16 Ma
2499±69 Ma
G Sample 15LX47-1
100 um
2500±18 Ma
#06
#12
#13
#24
2554±17 Ma
2542±18 Ma
2535±19 Ma
#25
#04
#30
2481±19 Ma
2444±17 Ma
2402±20 Ma
H Sample 15LX52-1
100 um
#09
#24
#28
2577±15 Ma
2546±15 Ma
2544±16 Ma
#25
#29
#22
2539±16 Ma
2497±66 Ma
2189±89 Ma
I Sample 15LX54-1
100 um
#09
#13
#01
2547±17 Ma
2546±17 Ma
2543±16 Ma
#26
#19
#23
2540±17 Ma
2521±17 Ma
2450±70 Ma

Figure 6

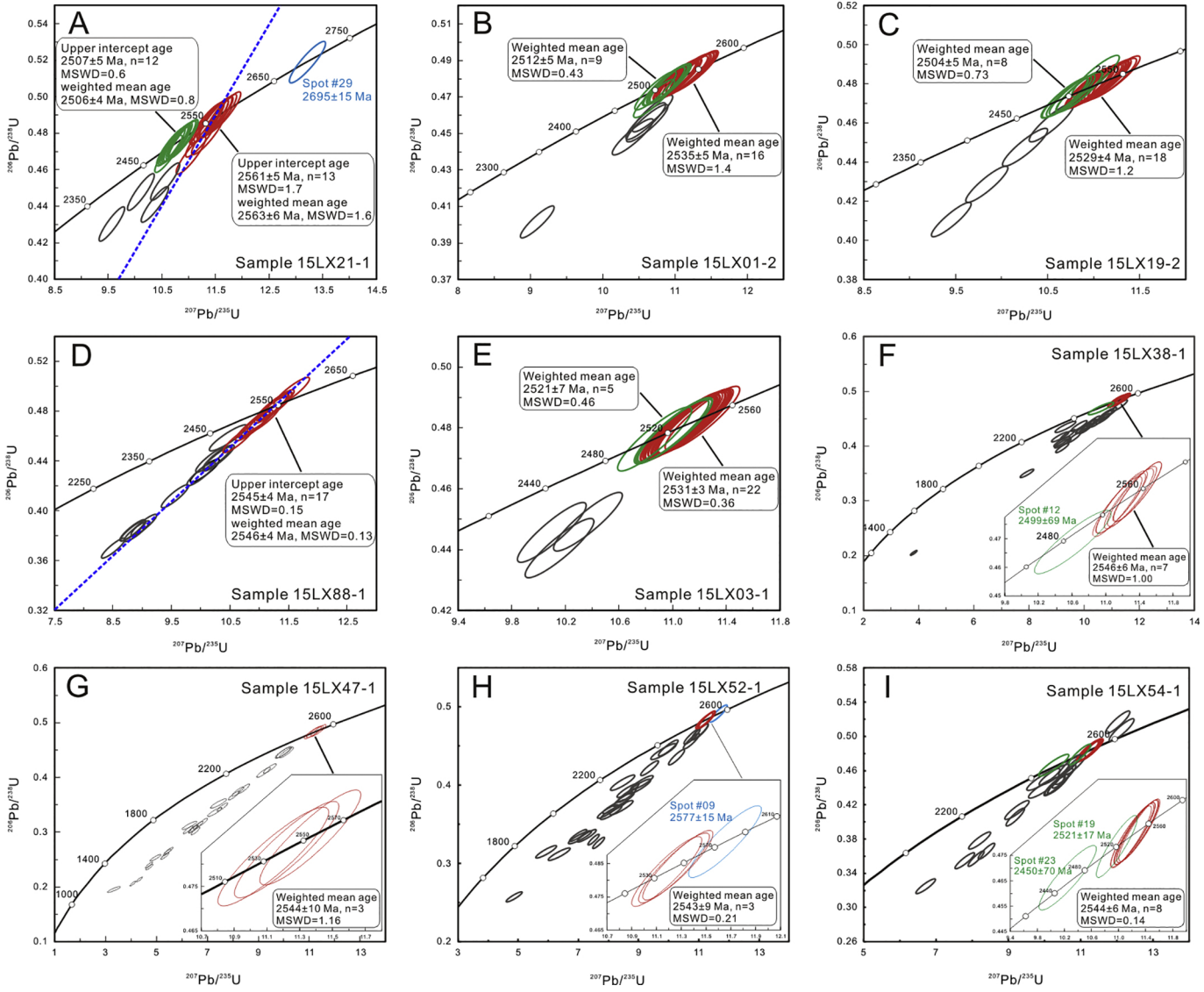
A
Upper intercept age
2507±5 Ma, n=12
MSWD=0.6
weighted mean age
2506±4 Ma, MSWD=0.8
Spot #29
2695±15 Ma
Upper intercept age
2561±5 Ma, n=13
MSWD=1.7
weighted mean age
2563±6 Ma, MSWD=1.6
Sample 15LX21-1
B
Weighted mean age
2512±5 Ma, n=9
MSWD=0.43
Weighted mean age
2535±5 Ma, n=16
MSWD=1.4
Sample 15LX01-2
C
Weighted mean age
2504±5 Ma, n=8
MSWD=0.73
Weighted mean age
2529±4 Ma, n=18
MSWD=1.2
Sample 15LX19-2
D
Upper intercept age
2545±4 Ma, n=17
MSWD=0.15
weighted mean age
2546±4 Ma, MSWD=0.13
Sample 15LX88-1
E
Weighted mean age
2521±7 Ma, n=5
MSWD=0.46
Weighted mean age
2531±3 Ma, n=22
MSWD=0.36
Sample 15LX03-1
F
Sample 15LX38-1
Spot #12
2499±69 Ma
Weighted mean age
2546±6 Ma, n=7
MSWD=1.00
G
Sample 15LX47-1
Weighted mean age
2544±10 Ma, n=3
MSWD=1.16
H
Sample 15LX52-1
Spot #09
2577±15 Ma
Weighted mean age
2543±9 Ma, n=3
MSWD=0.21
I
Sample 15LX54-1
Spot #19
2521±17 Ma
Spot #23
2450±70 Ma
Weighted mean age
2544±6 Ma, n=8
MSWD=0.14
$^{206}Pb/^{238}U$
$^{207}Pb/^{235}U$

Figure 7

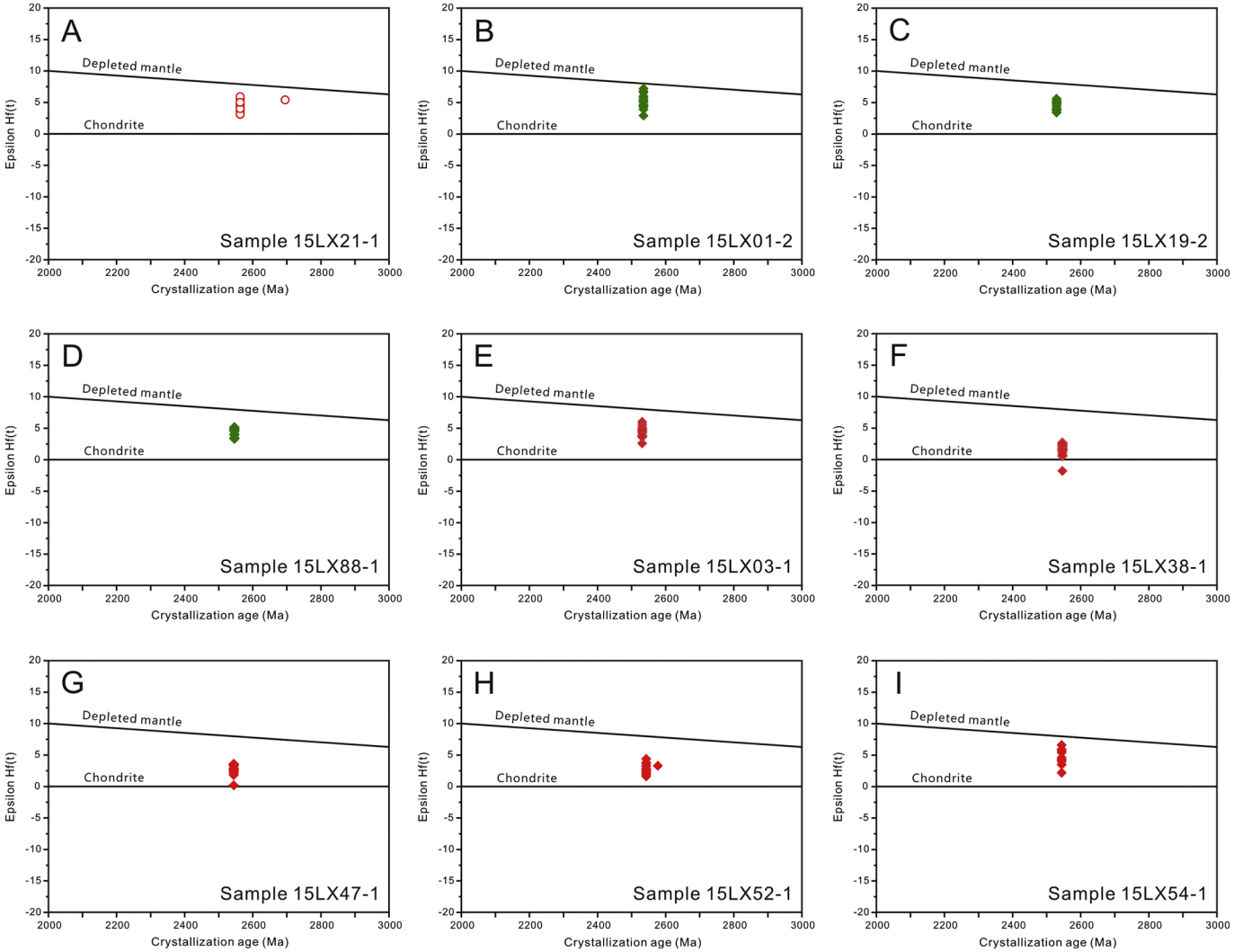
A
Depleted mantle
Chondrite
Sample 15LX21-1
B
Depleted mantle
Chondrite
Sample 15LX01-2
C
Depleted mantle
Chondrite
Sample 15LX19-2
D
Depleted mantle
Chondrite
Sample 15LX88-1
E
Depleted mantle
Chondrite
Sample 15LX03-1
F
Depleted mantle
Chondrite
Sample 15LX38-1
G
Depleted mantle
Chondrite
Sample 15LX47-1
H
Depleted mantle
Chondrite
Sample 15LX52-1
I
Depleted mantle
Chondrite
Sample 15LX54-1
Epsilon Hf(t)
Crystallization age (Ma)

Figure 8

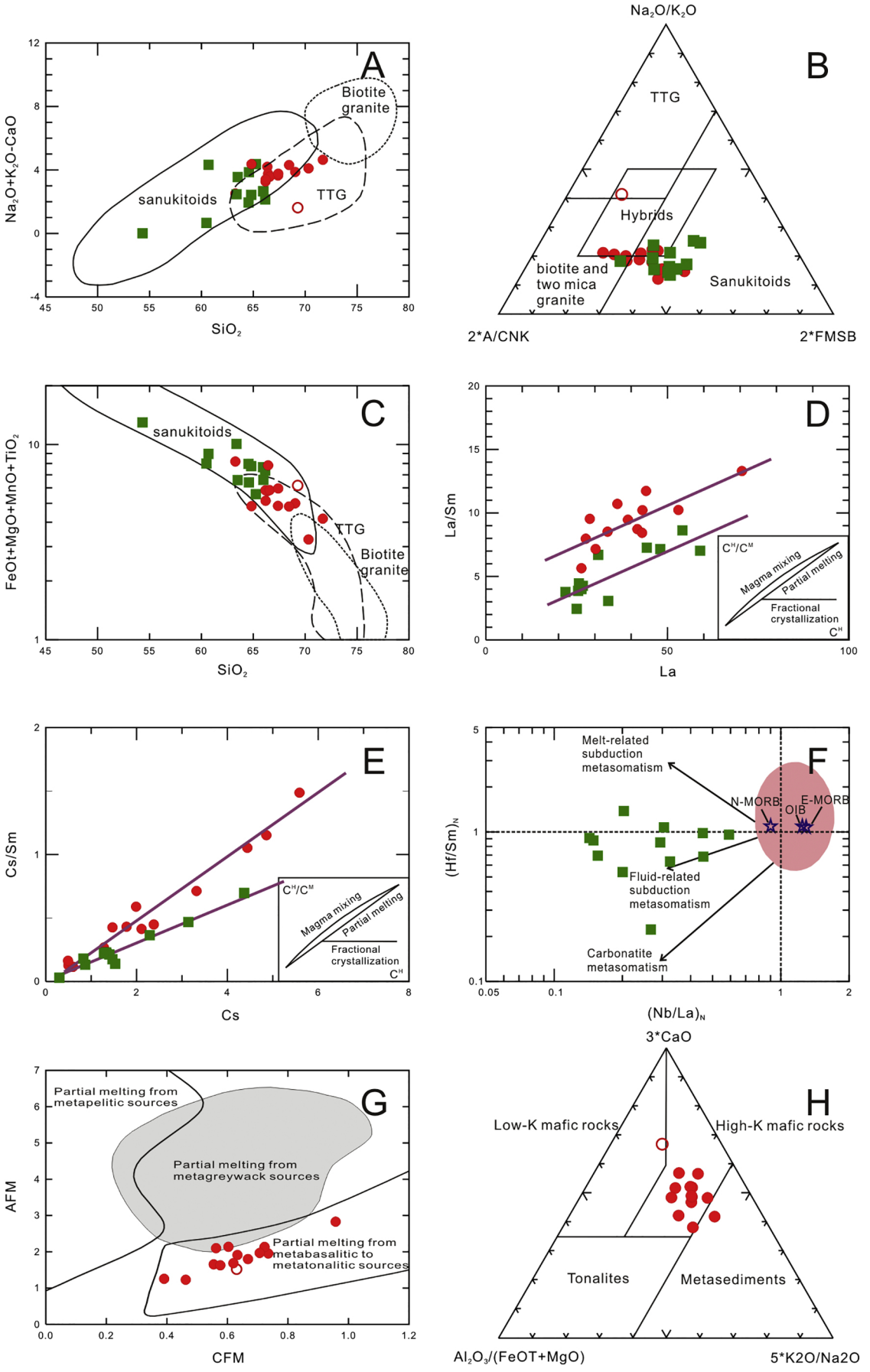
A
Biotite granite
sanukitoids
TTG
Na2O+K2O-CaO
SiO2
B
Na2O/K2O
TTG
Hybrids
biotite and two mica granite
Sanukitoids
2*A/CNK
2*FMSB
C
sanukitoids
TTG
Biotite granite
FeOt+MgO+MnO+TiO2
SiO2
D
La/Sm
La
CH/CM
Magma mixing
Partial melting
Fractional crystallization
CH
E
Cs/Sm
Cs
CH/CM
Magma mixing
Partial melting
Fractional crystallization
CH
F
Melt-related subduction metasomatism
N-MORB
E-MORB
OIB
Fluid-related subduction metasomatism
Carbonatite metasomatism
(Hf/Sm)N
(Nb/La)N
G
Partial melting from metapelitic sources
Partial melting from metagreywack sources
Partial melting from metabasalitic to metatonalitic sources
AFM
CFM
H
3*CaO
Low-K mafic rocks
High-K mafic rocks
Tonalites
Metasediments
Al2O3/(FeOT+MgO)
5*K2O/Na2O

Figure 9

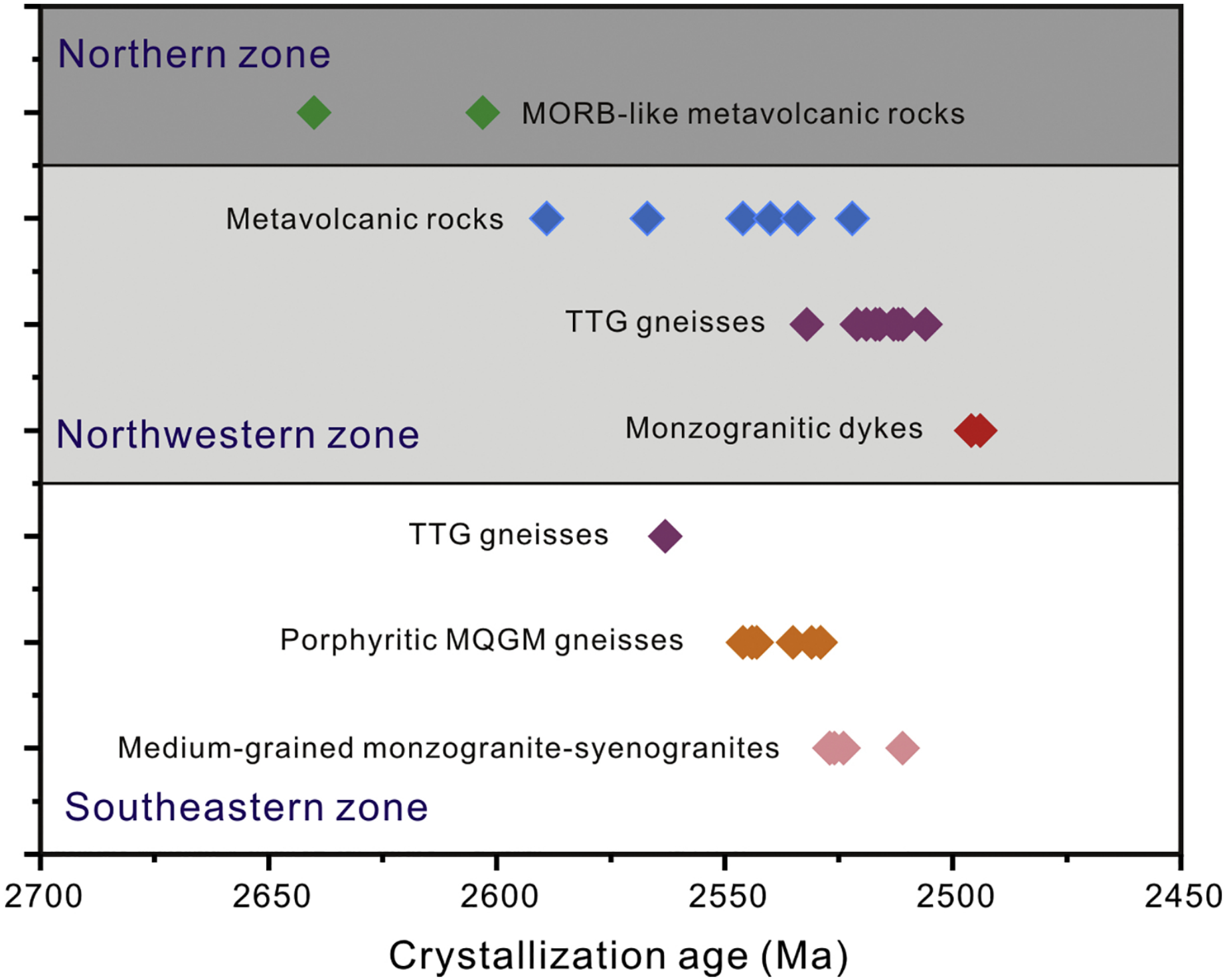
Northern zone
MORB-like metavolcanic rocks
Metavolcanic rocks
TTG gneisses
Northwestern zone
Monzogranitic dykes
TTG gneisses
Porphyritic MQGM gneisses
Medium-grained monzogranite-syenogranites
Southeastern zone
2700
2650
2600
2550
2500
2450
Crystallization age (Ma)

Figure 10

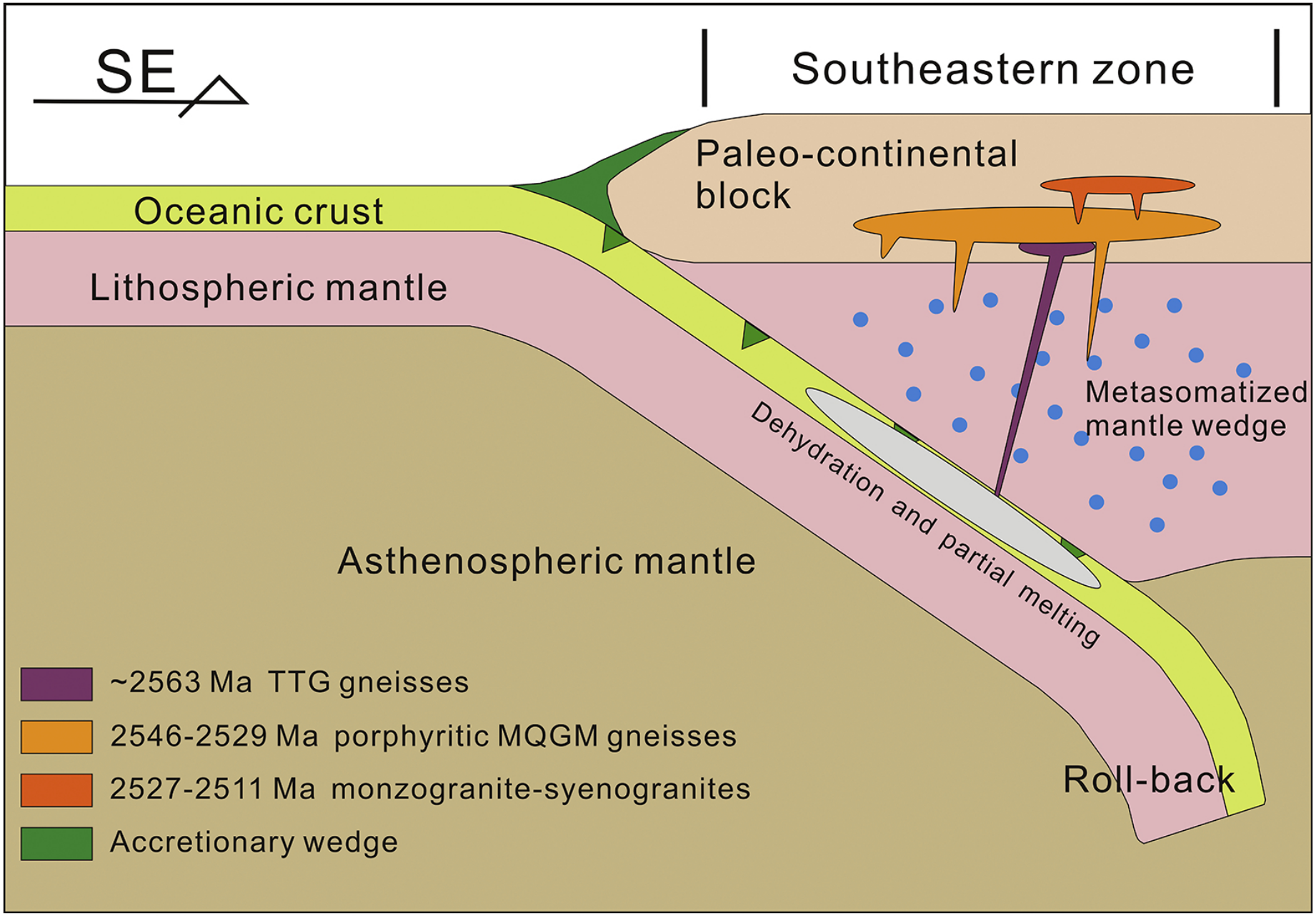
SE
Southeastern zone
Paleo-continental block
Oceanic crust
Lithospheric mantle
Metasomatized mantle wedge
Dehydration and partial melting
Asthenospheric mantle
~2563 Ma TTG gneisses
2546-2529 Ma porphyritic MQGM gneisses
2527-2511 Ma monzogranite-syenogranites
Accretionary wedge
Roll-back

Figure 11